ABSTRACT

Title of Thesis: FABRICATION OF AN ASYMMETRIC CERAMIC MEMBRANE VIA INDIRECT ADDITIVE MANUFACTURING

Patrick Gene Richard, Master of Science

Thesis Directed by: Professor, Dr. Dongxia Liu, Department of Chemical and Biomolecular Engineering
Professor, Dr. Nathan Lazarus, Army Research Lab, US

A dearth of literature regarding the fabrication of separation membranes via indirect additive manufacturing undermines the significant progress made by 3D technologies to improve resolution, printing time, and ease of operation. That is to say, the benefits of 3D printing may be realized even with an indirect route. This thesis aims to employ bench-scale stereolithography (SLA) to print a mold design that may be combined with a conventional technique to consistently yield viable alumina membrane supports for separation application. An iterative approach was applied to mitigate potential sources of variability, including poor mold design, mold casting, and ceramic substrate coating. Once the procedure was established, multiple alumina supports were fabricated, characterized, and coated with zeolite A(LTA) separation layers for pervaporation separations. The alumina supports demonstrated highly-ordered macroscopic structures, asymmetric microstructures, acceptable dimensional shrinkage (15.4%-18.5%), moderate density (2.89g/cm3), and good porosity (35.5%). The LTA-coated asymmetric membrane exhibited excellent separation performance with a flux of

0.800 kg/(m2•h) and a separation factor of 5190 for the pervaporation separation of an ethanol-water mixture. Although the generalizability is limited to other high-resolution bench-scale SLA printers, it is clear that high-quality ceramic separation membranes or substrates may be fabricated with an indirect additive manufacturing approach. Thus, the findings of this thesis provide a highly repeatable and reproducible fabrication pathway for challenging materials and geometries while still exploiting the unparalleled precision and control of 3D printing.

FABRICATION OF ASYMMETRIC CERAMIC MEMBRANES VIA INDIRECT ADDITIVE MANUFACTURING

by

Patrick Gene Richard

Thesis submitted to the Faculty of the Graduate School of the
University of Maryland, College Park, in partial fulfillment
of the requirements for the degree of
Master of Science
2022

Advisory Committee:
Professor Dongxia Liu, Chair
Professor Nathan Lazarus
Professor Chen Zhang
Professor Taylor J. Woehl

Dedication

I dedicate this to my mother, whose unwavering support and encouragement have and continue to impel me to accomplish more.

To Emily, without your tender care and generosity, I would not have completed this thesis.

Acknowledgements

I would like to thank Dr. Dongxia Liu for accepting me into her lab and guiding me throughout the research process. She worked with me to diagnose procedural shortcomings, edit my final thesis, and refine my presentation skills, all in an effort to prepare me to defend successfully.

I would like to thank Dr. Nathan Lazarus, who not only assisted in guidance but also educated me on good practices, nuances, and constraints associated with various 3D printing techniques. He also helped to advance my design ability in SolidWorks.

I would like to thank my senior graduate labmate, Akash Warty, for patiently assisting me with experiment design, answering my questions, and helping me to scrutinize new research directions.

I would also like to thank the individuals that contributed to specific aspects of my research. This includes Josh Tyler for printing mold designs and design brainstorming, Gaurav Iyer for density data procurement, Gordon Crago for providing access to a Form 2 SLA printer, Rebecca Fedderwitz for rheological data procurement, and Dr. Robert Bonenberger for compression data procurement.

I would like to thank my colleagues for creating an environment and forum to foster new ideas. Weekly meetings were invaluable as they sparked new thoughts and directions for my research.

Finally, I would like to thank Dr. Dongxia Liu, Dr. Nathan Lazarus, Dr. Chen Zhang, and Dr. Taylor Woehl for agreeing to serve on my thesis committee.

Table of Contents

List of Tables ……v

i

List of Figures ..... *vii*

Chapter 1: Introduction and Overview *1*

1.1. Background 1
1.1.1. Separations 1
1.1.2. Membranes 1
1.1.2.1. Alumina Membranes 2
1.1.3. Additive Manufacturing 3

1.2. Motivation and Objectives 5

1.3. Preliminary Limitations of The Study 7

1.4. Structure of Study 8

Chapter 2: Mold Design, Development, and Selection *10*

2.1. Designs 12
2.1.1. Movable Mold 12
2.1.2. Solid Cylindrical Mold 14
2.1.3. Mesh Cylindrical Mold-Helical Approach 15
2.1.4. Mesh Cylindrical-Alternative Approach 16

2.2. SLA 18
2.2.1. Printing of Movable Mold 19
2.2.2. Printing of The Solid Cylindrical Mold 20
2.2.3. Printing of Mesh Cylindrical Mold-Helical Approach 21
2.2.4. Printing of Mesh Cylindrical Mold-Alternative Approach 22

2.3. Analysis Of Casting Techniques 23
2.3.1. Colloidal Processing with Movable Mold 23
2.3.2. Colloidal Processing with Solid Cylindrical Mold 25
2.3.3. Pyrolysis 26
2.3.4. Colloidal Processing with Mesh Structure via Alternative Approach 27

2.4. Selection 31
2.4.1. Movable Mold 31
2.4.2. Solid Cylindrical Mold 31
2.4.3. Mesh Cylinder via Helical Approach 32
2.4.4. Mesh Cylinder Via Alternative Approach 32

2.5. Conclusions 33

Chapter 3: Fabrication of Alumina Substrate (Support) *34*

3.1. Introduction 34

3.2. Materials 34

3.3. Alumina substrate development 35
3.3.1. Slurry Development 35
3.3.2. Slurry Loading 40

3.3.3. Phase-Inversion/Solvent Extraction Via Immersion Precipitation....42
3.3.4. Demolding....44
3.3.5. Sintering....44
3.4. Properties of sintered alumina substrates....46
3.4.1. Macrostructure....46
3.4.1.1. Changes with Height....47
3.4.1.2. Digital Microscopy....48
3.4.2. Dimensions....49
3.4.2.1. Effect of Solid Loading....51
3.4.2.2. Effect of Holding Time....52
3.4.2.3. Effect of Sintering Temperature....53
3.4.3. Compressive Strength....54
3.4.3.1. Effect of Solid Loading....56
3.4.3.2. Effect of Sintering Temperature....56
3.4.3.3. Effect of Holding Time....57
3.4.4. Density....58
3.4.4.1. Effect of Solid Loading....59
3.4.4.2. Effect of Holding Time....60
3.4.4.3. Effect of Sintering Temperature....62
3.4.5. Porosity....63
3.4.5.1. Effect of Solid Loading....64
3.4.5.2. Effect of Holding Time....65
3.4.5.3. Effect of Sintering Temperature....67
3.4.6. Microstructure....68
3.4.6.1. Sintering Temperature....68
Effect of....69
3.4.6.2. Solid Loading....69
3.4.6.3. Cross Section....71
3.5. Conclusions....72
Chapter 4: LTA Composite Membrane for Ethanol-Water Pervaporation Separation 74
4.1. Introduction....74
4.2. Experimental....75
4.2.1. Materials....75
4.2.2. Zeolite Synthesis....76
4.2.3. Pervaporation Tests....76
4.2.4. Pervaporation Analysis....78
4.3. Results and Discussion....79
4.3.1. Independent Performance of Alumina Substrate....79
4.3.2. Performance of The Ceramic Membrane....79
4.3.3. Microscopic Analysis of Zeolite Deposition....81
4.4. Conclusions....83
Chapter 5: Conclusions and Future Work....85
5.1. Conclusions....85
5.2. Future Work....86
References 88

List of Tables

TABLE 1.1. CERAMIC MEMBRANES BASED ON PORE SIZE AND PERMEATION MECHANISM. ACRONYMS: NANONFILTRATION(NF),ULTRAFILTRATION(UF), MICROFILTRATION.(MF) ADAPTED FROM REF. 3 2

TABLE 2.1. COMPOSITION OF SLURRY USED IN INITIAL EXPLORATION OF MOLDS. 24

TABLE 2.2. FINAL DIMENSIONS FOR MESH CYLINDER VIA ALTERNATIVE APPROACH 33

TABLE 3.1. COMPOSITION OF ETHANOL/PVB/ALUMINA SYSTEM GIVEN IN WEIGHT PERCENTAGES.....37

TABLE 3.2 COMPOSITION OF NMP/PVB/ALUMINA SYSTEM GIVEN IN WEIGHT PERCENTAGES 38

TABLE 3.3. SHRINKAGE VALUES IN THE AXIAL, RADIAL OUTER DIAMETER AND RADIAL INNER DIAMETER DIRECTIONS FOR THE ENTIRE POPULATION OF SAMPLES.....50

TABLE 3.4. THE EFFECT OF VARYING SOLID LOADING ON THE ULTIMATE COMPRESSIVE STRENGTH OF ALUMINA MEMBRANES. COMPRESSIVE STRENGTH VALUES ARE AN AVERAGE FOR A GIVEN WEIGHT FRACTION.....56

TABLE 3.5. THE EFFECT OF VARYING SINTERING TEMPERATURE ON THE ULTIMATE COMPRESSIVE STRENGTH ALUMINA MEMBRANES. COMPRESSIVE STRENGTH VALUES ARE AN AVERAGE FOR A GIVEN SINTERING TEMPERATURE. 56

TABLE 3.6. THE EFFECT OF VARYING SINTERING HOLDING TIME ON THE ULTIMATE COMPRESSIVE STRENGTH ALUMINA MEMBRANES. COMPRESSIVE STRENGTH VALUES ARE AN AVERAGE FOR A GIVEN SINTERING HOLDING TIME.....57

TABLE 3.7. DESCRIPTIVE STATISTICAL INFORMATION REGARDING DENSITY FOR THE ENTIRE POPULATION OF SAMPLES 59

TABLE 3.8. DESCRIPTIVE STATISTICAL INFORMATION REGARDING POROSITY FOR THE ENTIRE POPULATION OF SAMPLES 64

TABLE 3.9 DESCRIPTIVE STATISTICAL INFORMATION REGARDING PORE SIZE DISTRIBUTION FOR DIFFERENT SOLID LOADINGS 71

TABLE 4.1 SEPARATION PERFORMANCE FOR ALUMINA SUPPORT 37 PRIOR TO ZEOLITE COATING 79

TABLE 4.2 SEPARATION PERFORMANCE FOR ALUMINA SUPPORT 37 AFTER ONE CYCLE OF ZEOLITE COATING.....80

TABLE 4.3 PERFORMANCE DATA FOR THE DEHYDRATION OF ETHANOL ON α-ALUMINA SUPPORTS FROM VARIOUS STUDIES 80

List of Figures

FIGURE 1.1 SCHEMATIC SUMMARY OF AM TECHNIQUES. ACRONYMS: STEREOLITHOGRAPHY (SLA), TWO-PHOTON POLYMERIZATION (TPP), CONTINUOUS LIQUID INTERFACE PRODUCTION (CLIP), SELECTIVE LASERSINTERING (SLS), FUSED DEPOSITION MODELLING (FDM), DIRECT WRITING ASSEMBLY (DWA), LAMINATED OBJECT MANUFACTURING (LOM), AND SELECTIVE DEPOSITION LAMINATION (SDL). ADAPTED FROM 9. 4

FIGURE 2.1. A GENERALIZED PROCESS FLOW DIAGRAM FOR MOLD DESIGN FABRICATION AND EXPLORATION. ORANGE-COLORED BOXES REPRESENT DECISION-MAKING STEPS OR BOTTLENECKS THAT CONTRIBUTE TO THE ITERATIVE NATURE OF THE PROCESS. 10

FIGURE 2.2. (A) SOLIDWORKS IMAGE OF THE OUTER CYLINDER OF THE MOVABLE MOLD. OUTER SURFACE OF OUTER CYLINDER IS 11.43 MM. THE OUTER CYLINDER IS 2 MM THICK. THE THIN CYLINDER IN THE CENTER IS USED TO ANCHOR THE DETACHED INNER CYLINDER (B) SOLIDWORKS IMAGE OF THE INNER CYLINDER WITH ATTACHED BASE. INNER CYLINDER HAS A DIAMETER OF 6.35 MM AND LENGTH OF 25.4 MM. 13

FIGURE 2.3. SOLIDWORKS IMAGE OF COMPLETED SOLID CYLINDRICAL MOLD. THICKNESS OF THE ANNULUS IS 1.875 MM; DIAMETER OF THE INNER ROD IS 6.35 MM. OUTER DIAMETER OF THE OUTER CYLINDER IS 12.19 MM. 15

FIGURE 2.4. SOLIDWORKS IMAGE OF MESH CYLINDER DESIGNED VIA HELICAL APPROACH INNER CYLINDER DIAMETER IS 6.35 MM. 16

FIGURE 2.5. SOLIDWORKS IMAGE OF MESH CYLINDER DESIGNED VIA ALTERNATIVE APPROACH. THE OUTER DIAMETER OF THE OUTER INNCER CYLINDER 9.65 MM. THE OUTER DIAMETER OF THE INNER ROD IS 6.35 MM. THE AREA OF THE HOLES IS 1.52 MM. 17

FIGURE 2.6. AN IMAGE OF THE FORM2, WHICH HAS A BUILD VOLUME OF 145X145X175MM. IT IS FORMLABS' SECOND-GENERATION DESKTOP PRINTER AND WAS USED TO PRINT THE DESIGNS PRESENTED IN THIS STUDY.[16] 18

FIGURE 2.7. FINISHED MOVABLE MOLD AFTER PRINTING WITH FORMLABS STANDARD HIGH-TEMPERATURE V2 RESIN AND POST-PROCESSING. THE OUTER AND INNER CYLINDER ARE SHOWN TOGETHER TO DEMONSTRATE HOW THE MOLD WILL BE USED. 20

FIGURE 2.8. FINISHED SOLID CYLINDRICAL MOLD AFTER PRINTING WITH FORMLABS STANDARD HIGH-TEMPERATURE V2 RESIN AND POST-PROCESSING. THE SOLID CYLINDRICAL MOLD WAS PRINTED WITH HIGH ACCURACY AND SMOOTH FINISHES. 21

FIGURE 2.9. FINISHED MESH MOLD VIA HELICAL APPROACH AFTER PRINTING WITH FORMLABS STANDARD HIGH-TEMPERATURE V2 RESIN AND POST-PROCESSING. CONSIDERABLE HOLE CLOSURE WAS OBSERVED. 22

FIGURE 2.10. FINISHED MESH MOLD VIA ALTERNATIVE APPROACH AFTER PRINTING WITH FORMLABS STANDARD CLEAR V2 RESIN AND POST-PROCESSING. VIRTUALLY NO HOLE CLOSURE WAS OBSERVED. 23

FIGURE 2.11. THREE SEPARATE TRIALS OF COLLOIDAL PROCESSING WITH THE MOVABLE MOLD. (A) GREEN BODY IS SLIGHTLY LONGER THAN DESIRED.(B) MOST ACCURATE GREEN BODY OF THE TRIAL. HOWEVER, RIGHT END IS THINNER. (C) GREEN BODY WAS SEVERELY DEFORMED. 24

FIGURE 2.12. IMAGE OF SOLID CYLINDRICAL MOLD AFTER COMPLETING SINTERING PROFILE WHILE SUBJECTED TO 200ML/MIN AR FLOW. THE SOLID CYLINDRICAL MOLD CONVERTED TO GLASSY CARBON BUT DID NOT RETAIN SHAPE. 27

Figure 2.13. Isolated alumina green body after completing phase-inversion via immersion precipitation and demolding.....28

Figure 2.14. Image of mold/slurry composite immersed in DI water while slurry undergoes phase-inversion to form membrane. The surrounding white material is alumina that has leached from the slurry.....29

Figure 2.15. TGA data comparing tubular and hollow fiber green bodies. TAM refers to the tubular alumina membrane that experienced leaching. HFM refers to the hollow fiber membrane known to undergo successful sintering.....30

Figure 3.1. Terpolymer structure of PVB. Image is adapted from ref 38.....37

Figure 3.2. Alumina membrane green body from NMP/PVB/Alumina slurry. The slurry resulted in better filling which in turn led to better shape retention of the mold. However, there are large holes, surface defects, and slight tilt.....39

Figure 3.3. Rheological data for slurries with alumina weight fraction of 0.60.(A) Shear-controlled data with viscosity and stress as response variables. (B) Stress-controlled data with viscosity and shear rate as outputs. Both plots indicate shear-thinning behavior.....40

Figure 3.4. Schematic demonstrating the effect of adding a lubricant on the interaction between two solid surfaces. Adapted from ref. 42.....41

Figure 3.5. Ternary phase diagram of polymer, solvent, non-solvent with a representative pathway of binodal demxing. Adapted from ref 45.....43

Figure 3.6. Sintering profile used to fabricate alumina membranes.....45

Figure 3.7 Images of Sintered Alumina Supports. (A) Similarities between sintered alumina supports lengthwise. (B) Similarities between sintered alumina supports radially.....46

Figure 3.8 Sintered alumina supports at the three different heights (25.4 mm, 50.8 (2 in) mm, and 76.2 mm (3in)) explored.....47

Figure 3.9 Images from digital microscopy for specimen UID 7. (A) Outer surface with highly ordered pattern. (B) Bottom radial cross-section. (C) Top radial cross-section. (D) Close-up of outer surface with highly ordered pattern.....48

Figure 3.10.The effect of alumina weight fraction on dimensional shrinkage in the (A) axial direction, (B) radial direction for the outer diameter, and (C) radial direction for the inner diameter. Values provided are an average at a weight fraction.....51

Figure 3.11. The effect of sintering holding time on dimensional shrinkage in the (A) axial direction, (B)radial direction for the outer diameter, and (C) radial direction for the inner diameter. Values provided are an average at a given holding time.....52

Figure 3.12. The effect of sintering temperature on dimensional shrinkage in the (A) axial direction, (B)radial direction for the outer diameter, and (C) radial direction for the inner diameter. Values provided are an average at a given sintering temperature.....53

Figure 3.13. Image of compression test setup to determine ultimate compressive strength. The top platen travels at a speed of 1 mm/min.....55

FIGURE 3.14 DENSITY AS A FUNCTION OF ALUMINA SOLID LOADING IN CASTING SLURRY. VALUES ARE AVERAGES FOR GIVEN WEIGHT FRACTION....59

FIGURE 3.15. DENSITY VS. CHANGES IN HOLDING TIME. VALUES ARE AVERAGES FOR GIVEN HOLDING TIME. 61

FIGURE 3.16. DENSITY VS. CHANGES IN SINTERING TEMPERATURE. VALUES ARE AVERAGES FOR GIVEN SINTERING TEMPERATURE. 62

FIGURE 3.17. POROSITY AS A FUNCTION OF ALUMINA SOLID LOADING IN CASTING SLURRY. VALUES ARE AVERAGES FOR GIVEN WEIGHT FRACTION....65

FIGURE 3.18. POROSITY VALUES VS. CHANGES IN HOLDING TIME. VALUES ARE AVERAGES FOR GIVEN HOLDING TIME AT A FIXED SINTERING TEMPERATURE OF 1500. 66

FIGURE 3.19. POROSITY VALUES VS. CHANGES IN SINTERING TEMPERATURE. VALUES ARE AVERAGES FOR GIVEN SINTERING TEMPERATURE AT A FIXED HOLDING TIME OF 6 HOURS 67

FIGURE 3.20 SEM IMAGES OF THE INNER SURFACE WITH CHANGES IN TEMPERATURE FROM (A) 1500 °C, (B) 1550 °C, AND (C) 1600 °C IMAGES WERE OBTAINED 5.0K MAGNIFICATION....69

FIGURE 3.21 SEM IMAGES OF OUTER SURFACES AT (A)0.50 SOLID LOADING, (B) 0.55 SOLID LOADING, (C) 0.60 SOLID LOADING. IMAGES WERE OBTAINED AT 5.0K MAGNIFICATION. 70

FIGURE 3.22. RADIAL CROSS-SECTION AT MAGNIFICATIONS OF (A) 50X AND (B) 2500X. 71

FIGURE 3.23 SCHEMATIC OF FABRICATION PROCEDURE. 72

FIGURE 4.1 LAB-SCALE SCHEMATIC OF THE PERVAPORATION PROCESS. ADAPTED FROM REF. 7 74

FIGURE 4.2 SCHEMATIC OF PERVAPORATION SETUP. 77

FIGURE 4.3 SEM IMAGES OF COATED AND BARE SUBSTRATES. (A) OUTER SURFACE OF COATED SUPPORT UID 37, (B) INNER SURFACE OF COATED SUPPORT UID 37,(C) OUTER SURFACE OF BARE SUPPORT UID 38,(D) INNER SURFACE OF BARE SUPPORT UID 38. ALL IMAGES WERE OBTAINED AT 10.0K MAGNIFICATION WITH THE EXCEPTION OF (B) WHICH WAS OBTAINED AT 4.99K MAGNIFICATION. 82

Chapter 1: Introduction and Overview

1.1. Background

1.1.1. Separations

A number of environmental concerns, such as air pollution and water contamination, have become increasingly pervasive and necessitate novel solutions to mitigate their effects. Many of these concerns may be combated with separation methods. Separations, which encompass purification and concentration processes, are integral components to many industrial chemical plants, and as a result, many of a plant's resources are allocated to these separation operations. Bin Liang and colleagues cited that over 50% of a plant's energy usage is appropriated to these operations.[1] The impact of these processes is not confined to chemical plants alone, as David Sholl's group communicated in "Seven Chemical Separations to Change The World." Sholl's group stated that 10% to 15% of the United States' total energy consumption was attributed to separations.[2] They postulate that if more energy-efficient methods were employed for these separations in the U.S., a 100 million tonnes reduction in carbon dioxide emissions and a 4 billion dollar decrease in energy could be realized.[2] [2]

1.1.2. Membranes

Membrane separation is the selective removal of materials in a mixture by allowing components to permeate across the membrane while others remain in the feed. Efficient separations typically exploit differences in the size of the species or the chemical potential across the membrane. Membrane separations have often been lauded as energy-efficient alternatives to conventional operations. They bear several more advantages over

conventional separations, including facile operation, small footprint, and high separation.[3] They are employed in various applications, including gas separations, carbon capture and sequestration, desalination, and solvent purification. Applications with harsh conditions or swelling concerns, for instance, are more aptly addressed with ceramic membranes.

Ceramic membranes are composed of metal oxides such as alumina (Al_2O_3), titania (TiO_2), zeolites (i.e., aluminosilicate), non-metal oxides such as carbides and nitrides, or some combination of oxides and non-oxides. Ceramic membranes are typically asymmetric with varying porosity layers. Table 1.1 classifies ceramic membranes based on pore size.

Table 1.1. Ceramic membranes based on pore size and permeation mechanism. Acronyms: Nanonfiltration(NF),Ultrafiltration(UF), Microfiltration.(MF) Adapted from ref. 3

Porous Membrane	Pore Size Diameter, nm	Applications	Permeation Mechanism	Advantages/Disadvantages
Microporous	<2	Gas separation + NF	Molecular sieving	Low pore size diameter with a potential use in molecular sieve separation
Mesoporous	2–50	NF + UF and gas separation	Knudsen diffusion	High permeability and low selectivity. Used in the synthesis of composite membranes.
Macroporous	>50	UF/MF	Poisseuille flow	High permeability as a support in the synthesis of composite membranes, or as a distributor of reagents

Table 1.1 demonstrates the versatility and tunability of ceramic membranes as they cover an extensive range of pore sizes and accommodate several different applications.

1.1.2.1. Alumina Membranes

Of the ceramic membranes, alumina has garnered increased attention. In addition to the chemical and physical stability characteristic of ceramic materials, alumina demonstrates extreme hardness, electrical resistivity, and corrosion resistance.[4]These advantages have led to the use of alumina membranes in water treatment, food

processing, and pharmaceuticals. Thus, alumina has developed a niche where quality is of the utmost importance. Even with these desirable traits, alumina membranes have failed to gain ubiquity because fabrication is a costly, complicated multi-step process with low reproducibility.[5–7]Fortunately, the burgeoning field of additive manufacturing or 3D printing seems well-equipped to help eliminate or, at the very least, mitigate the shortcomings associated with alumina membrane fabrication.

1.1.3. Additive Manufacturing

Additive manufacturing is the deposition of material, layer-by-layer, along a computer-aided design (CAD) path. Additive manufacturing techniques are broadly categorized under four types: photopolymerization, powder, material extrusion, and lamination. Figure 1.2 provides examples of each technique, along with schematics of operation. Of these techniques, photopolymerization is the best equipped, at this time, to handle the fabrication of separation membranes, owing to its high resolution. For example, Matthias Wessling's group has succeeded with photopolymerization techniques as they were able to print polydimethylsiloxane (PDMS) membranes with direct light processing (DLP) printing.[8] DLP is similar to SLA, but it uses a DLP projector to generate cross-sections rather than a UV laser. Wessling and colleagues' success notwithstanding, direct printing of separation membranes has achieved limited success overall and significantly less with inorganic and alumina membranes.

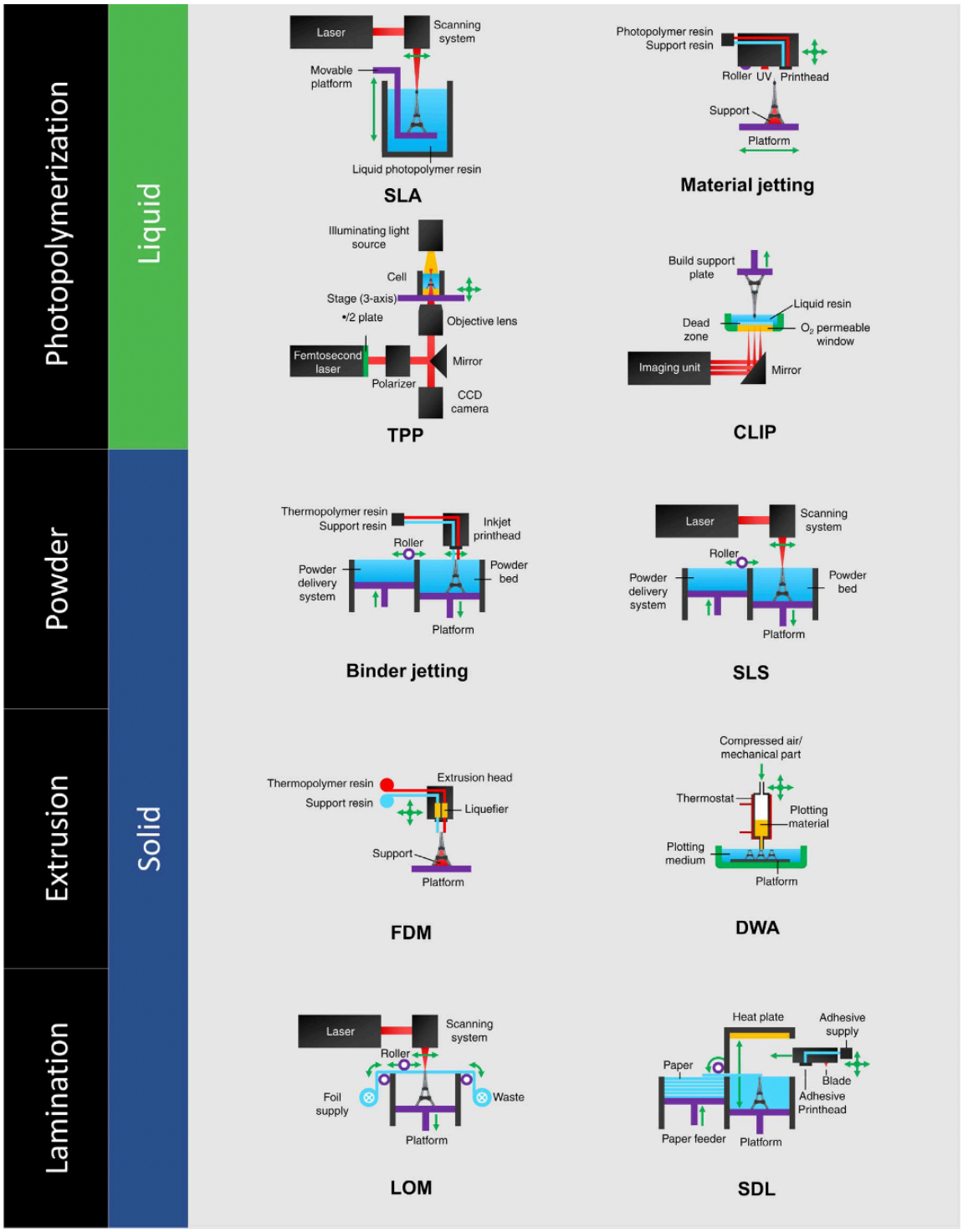

Figure 1.1 Schematic summary of AM techniques. Acronyms: stereolithography (SLA), two-photon polymerization (TPP), continuous liquid interface production (CLIP), selective lasersintering (SLS), fused deposition modelling (FDM), direct writing assembly (DWA), laminated object manufacturing (LOM), and selective deposition lamination (SDL). Adapted from 9.

1.2. Motivation and Objectives

Currently, research efforts for the additive manufacturing of alumina membranes have been focused primarily on direct fabrication.[9–11] Although direct printing of the membrane is ideal, developing a mixture composition that is compatible with a given technique is a non-trivial endeavor primarily because of resolution and material limitations.[9–11] The pursuit to directly fabricate alumina membranes has resulted in a lack of exploration of indirect methods. This potentially undermines and ignores the significant advancements many printing techniques have made to improve resolution, printing time, and surface finishes.[9] Such improvements could potentially yield a robust mold that in turn improves the final structural characteristics of the alumina membrane. Thus, a failure to explore improved 3D technologies and indirectly implement them into membrane fabrication has limited researchers from truly exploiting all aspects of 3D printing.

This paper seeks to assert that the benefits of 3D printing may be realized even with an indirect fabrication route. That is to say, even as a complement to a conventional technique,3D printing may not only simplify but also enhance the repeatability and reproducibility of the fabrication procedure. To illustrate this impact of 3D printing, the objectives of the study and implied research questions are the following:

1. Envisage and design a mold that is theoretically compatible with a conventional technique (e.g., Phase Inversion or Slip-Casting). This objective will address the following questions: (a)What are the possible designs, (b) with what software will the mold design be constructed, and (c)how must the mold be designed to ensure compatibility?

2. Print the mold design with a 3D printing technique with high accuracy and consistency. The following research questions will be answered:(a) what printing technique will be employed, (b) how do the advantages of this printing technique accommodate conceived designs, and(c) what elements of design will affect printing viability?

3. Preliminarily employ a conventional technique to determine if mold is capable of yielding an alumina membrane. This objective will address the following questions:(a) what conventional techniques are available, (b) how will these techniques be executed, (c) do these techniques yield near-net shapes, and (d) what determines successful application?
4. Develop a facile highly repeatable and reproducible procedure to fabricate an alumina membrane using the mold. This objective will address the following questions:(a) what is the final alumina concentration in the casting solution (b) how is the concentration determined, (c) how the membrane matrix is obtained, (d) how the alumina membrane is demolded, (e) how is the alumina densified, and (f) what are the desired morphological characteristics?
5. Characterize the alumina membrane and use this data to highlight the effects of 3D printing. The following research questions will be answered:(a) what are the methods of characterization, (b)what do the results of these characterizations imply about the membrane, (c) are there any discernable trends, (d) are these trends consistent with literature, and (e) what is the added value of using 3D printing?

6. Use the alumina membrane as a support in a practical separation process and analyze its performance. This objective will address the following questions:(a) what separation process will be explored, (b) why is the alumina membrane used for this process, (c) what will be used as the separation layer, and (d) what is the interplay between support and separation layer?

This study will contribute to the knowledge of available lab-scale alumina membrane fabrication techniques by offering a novel indirect fabrication route that exploits 3D printing. Furthermore, it will discuss how indirect 3D printing can help to control membrane characteristics and how that can impact the deposition of a separation layer. [5] This will help to address the current shortage of research in this area and serve as a reference for the continued exploration of additive manufacturing with alumina, as well as, ceramics.

1.3. Preliminary Limitations of The Study

This section will present the limitations that were apparent at the beginning of this study by discussing the scope, availability of resources, and generalizability of findings.

The scope of this study is confined to the lab-scale fabrication of alumina membranes. That is to say, a great deal of development of 3D printing techniques and additional research must occur before considering scaling-up.[9–11] Also, the research methodology is more concerned with reducing complexity rather than cost as comparative estimates are difficult to quantify. This analysis may appear subjective, but it will be presented through the perspective of critical process parameters.

Experiments in this study were executed by two graduate-level students in about 1 year. Students have a developing knowledge of complex topics employed such as zeolite synthesis and quaternary component mass transfer. However, these are topics that take several years of experience to fully grasp.

Physical access to various printing techniques was also limited, which in turn restricts the generalizability of the findings to the printing technique employed in this study. In other words, because there are over 50 printing techniques available and this study only explores one, it would be incorrect to say indirect fabrication is similarly impactful with other printing techniques.[9,10]

1.4. Structure of Study

Now that the motivation, objectives, and limitations have been established, this section will provide an overview of the content to be presented in the upcoming chapters. Chapter 2 will discuss objectives 1, 2, and 3 along with the underlying research questions. This will provide insight to the evolution and selection of the final mold design. Chapter 3 will address objectives 4 and 5 along with the underlying research questions. It will discuss how the process parameters were manipulated to establish the final methodology. Additionally, it will discuss the impact of 3D printing on the final membrane properties. Chapter 4 will address objective 6 along with the underlying research questions. It will discuss whether the alumina membranes are viable functional supports. It will also discuss how 3D printing and resulting surface morphology impact the formation and performance of the separation layer. Chapter 5 will conclude the study with a final assessment of important findings and discussion on how these findings can

potentially lay the foundation for further exploration of alumina membrane fabrication with additive manufacturing.

Chapter 2: Mold Design, Development, and Selection

In this chapter, the iterative procedure of designing and developing a suitable mold is discussed. A generalized process flow diagram from design idea to preliminary fabrication methods is provided in Figure 2.1

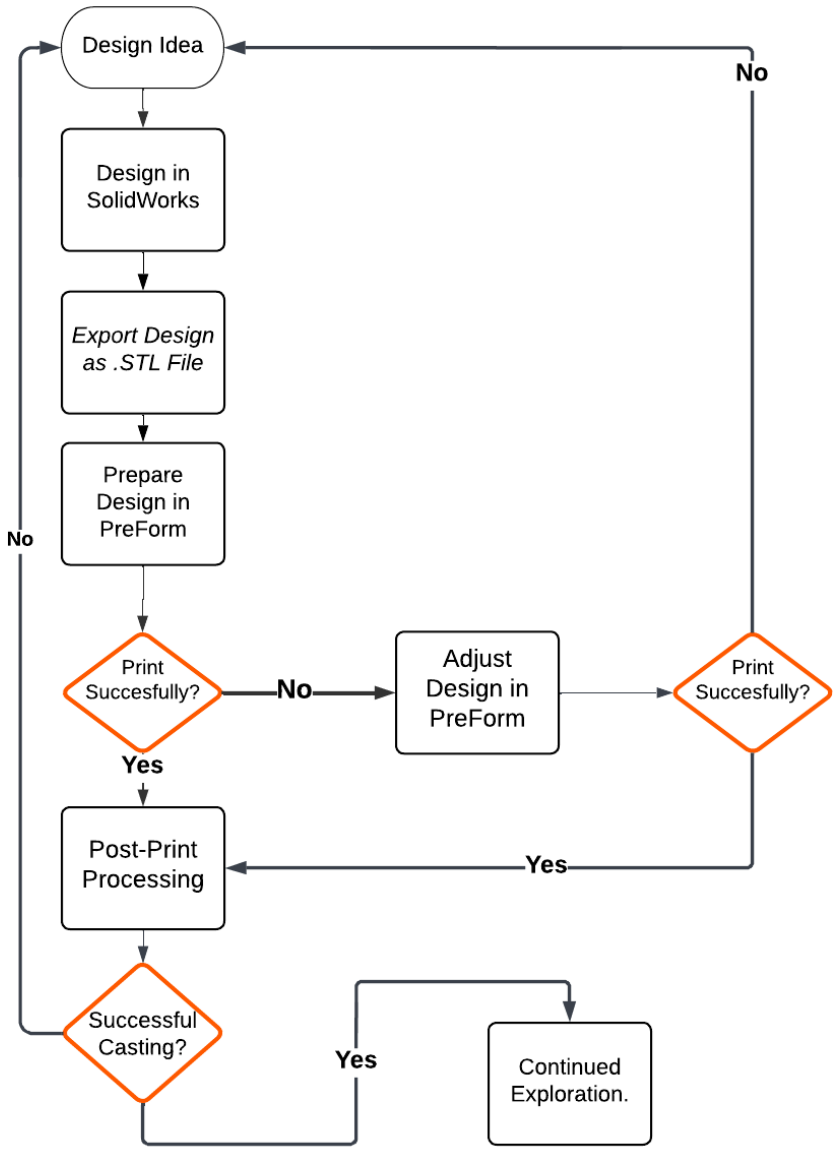

Figure 2.1. A generalized process flow diagram for mold design fabrication and exploration. Orange-colored boxes represent decision-making steps or bottlenecks that contribute to the iterative nature of the process.

Figure 2.1 presents the initial exploration process to fabricating an alumina substrate that will lay the foundation for finalizing and optimizing the procedure in chapter 3. Admittedly, there is some overlap between chapters as casting techniques must be employed to determine mold viability, but the interpretations will change. For instance, "Successful Casting" in Figure 2.1 and chapter 2 as a whole, refers to the ability of the mold to simply isolate an alumina substrate; whereas, in chapter 3, it will refer to attaining specific properties on the final sintered support. In other words, although the discussion of casting techniques overlaps, the focus of chapter 2 is on the mold, and the focus of chapter 3 is on the support itself. It is important to bear this distinction in mind as it will elucidate the rationale behind the decision-making in this chapter.

As communicated in the introduction, this chapter will address objectives 1,2, and 3, and the structure of this chapter will mirror as such. Thus, the first section will discuss the designs explored and their construction. Secondly, the efficacy of these designs to be printed with stereolithography will be assessed and presented. Then, a discussion of preliminary casting techniques employed to fabricate an alumina support will be offered. Finally, the chapter will culminate with the selection of the mold design that best satisfies the following criteria:

- The design must print accurately and consistently.
- The mold must present a pathway to yield an isolated alumina substrate.
- The alumina substrate should be near-net shape.
- The pathway must provide promise of achieving high repeatability and reproducibility.

2.1. Designs

This section will briefly describe how conceived supports were transposed to 3D digital renderings. It will delineate procedure, impetus, and intended usage for each design.

All mold designs were cylindrical and concave so that material could be cast to yield supports with tubular configurations. Tubular configurations are attractive because of their good fouling resistance and high cleaning efficiency.[12] Moreover, the tubular configuration was selected because it was intriguing enough to explore with 3D printing and likely the most feasible of configurations. For instance, a hollow fiber configuration would likely exceed the aspect ratio constraints of the printer, and a flat-sheet configuration would fail to show the ability to fabricate complex geometries.[13,14]

All designs were constructed using SolidWorks 2022. Once the designs were completed, they were exported as .STL files.

2.1.1. Movable Mold

On the top plane, two concentric circles were drawn. The innermost circle had a diameter of 9.40 mm (0.37 in), and the outermost circle had a diameter of 11.43 mm (0.45 in). These diameters corresponded to a thickness of approximately 2 mm (0.08 in). Using “extruded boss/base,” the sketch of concentric cylinders was projected along the z-axis to a height of 25.4 mm (1 in). At the top of the outer cylinder, using the “reference geometry” feature, a new plane was created. Thereafter, the new plane was used to sketch a circle with a diameter of 6.60 mm (0.26 inch). Then, using the “extrude-thin” feature, the circle was simultaneously projected to a height of approximately 1 mm (0.04 inch)

and given a thickness of 0.25 mm (0.01 inch). Once the cylinder was completed, a new plane perpendicular to an arbitrary point on the curved surface was generated. This plane was used to generate a fin that extended from the center cylinder to the top of the outer cylinder. Using the "circular pattern" feature, multiple copies of the fin were created around the center cylinder, and the design was completed, as seen in Figure 2.2(A). To complete the mold, a separate non-attached solid cylinder with a base was also designed. The non-attached cylinder was constructed with two separate extruded boss/base steps. The base was designed to have a diameter of 8.89 mm (0.35 in), and the inner cylinder had a diameter of 6.35 mm (0.25 in) and was projected to a height of 25.4 mm, as shown in Figure 2.2(B).

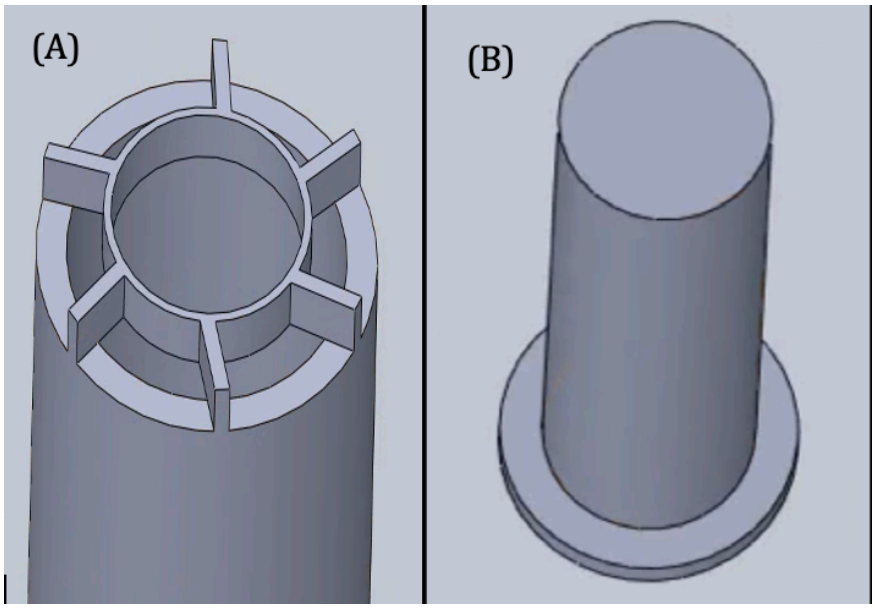

Figure 2.2. (A) SolidWorks image of the outer cylinder of the movable mold. Outer surface of outer cylinder is 11.43 mm. The outer cylinder is 2 mm thick. The thin cylinder in the center is used to anchor the detached inner cylinder (B) SolidWorks image of the inner cylinder with attached base. Inner cylinder has a diameter of 6.35 mm and length of 25.4 mm.

The mold design was conceived as a means to simulate wet-spinning phase inversion. The movable mold's outer cylinder was designed to anchor the inner cylinder without being permanently attached, hence the center cylinder with attached fins. Additionally, the base of the inner cylinder was designed to be slightly smaller than the inner walls of the outer cylinder. This design would allow the inner cylinder to slide through the outer cylinder and extrude the material, rendering the movable mold a candidate for colloidal processing.

2.1.2. Solid Cylindrical Mold

The solid cylindrical mold was constructed by, firstly, drawing a circle of 12.19 mm (0.48 in) on the top plane. Using extruded boss/base, the circle was projected along the z-axis to a height of 27.94 mm (1.10 in). Then, using the SolidWorks built-in “shell” feature, the top face of the cylinder was selected, and 10.16 mm (0.40 in) of this fully solid cylinder was rendered hollow, which corresponded to an outer cylinder thickness of approximately 1 mm. Also, using the shell feature, the bottom face was selected under the option multi-thickness to control the depth of the shell. From the top of the cylinder to the newly developed base, this hollow region had a depth of 25.4 mm (1 in). A new sketch was initiated on the positive z-face of the base. This sketch was used to draw a circle with a diameter of 6.35 mm (0.25 in) that would later be extruded to a height of 25.4 mm, as shown in Figure 2.3.The resulting thickness of the annular cavity was 1.875 mm (0.075 in).

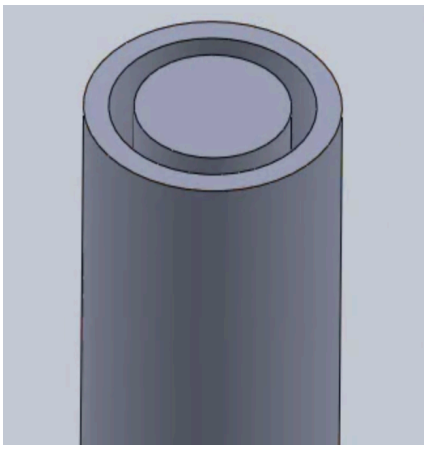

Figure 2.3. SolidWorks image of completed Solid Cylindrical Mold. Thickness of the annulus is 1.875 mm; Diameter of the inner rod is 6.35 mm. Outer diameter of the outer cylinder is 12.19 mm.

The solid cylindrical mold was explored with colloidal processing techniques and pyrolysis.

2.1.3. Mesh Cylindrical Mold-Helical Approach

The first step in constructing the mesh cylindrical mold via the helical approach was to sketch a rectangle on the top plane. The size of the rectangle was arbitrary and relatively unimportant as long as it was large enough to fit a circle with a diameter of 10.16 mm. Once the rectangular sketch was complete, it was projected using extruded boss/base, and a circle with a diameter of 10.16 mm was drawn on the positive z-face of the rectangular prism. Using the "curves" feature, a spiral/helix curve was drawn in the positive z-direction. This spiral/helix curve eventually served as a path for subsequent features. At an arbitrary point along the circumference of the circle, circular cross-sections were drawn. Then using the circular pattern feature for sketches, multiple copies of the cross-section were populated around the circle. Using the "sweep" feature, the cross-sections were projected in the positive z-direction along the path of the spiral. At the top of these projections, a new plane was created using the reference geometry

feature. On this plane, the exact same procedure of sketching a circle, establishing a helical/spiral path, and sweeping the cross sections was executed. The only exception was that the path and, therefore, the sweeps were oriented in negative z-direction. The result was a number of interconnecting cylinders comprising the outer cylinder. An inner cylinder with a diameter 6.35 mm was added to the center of the base to ensure cast parts would be hollow. The completed design is given in Figure 2.4.

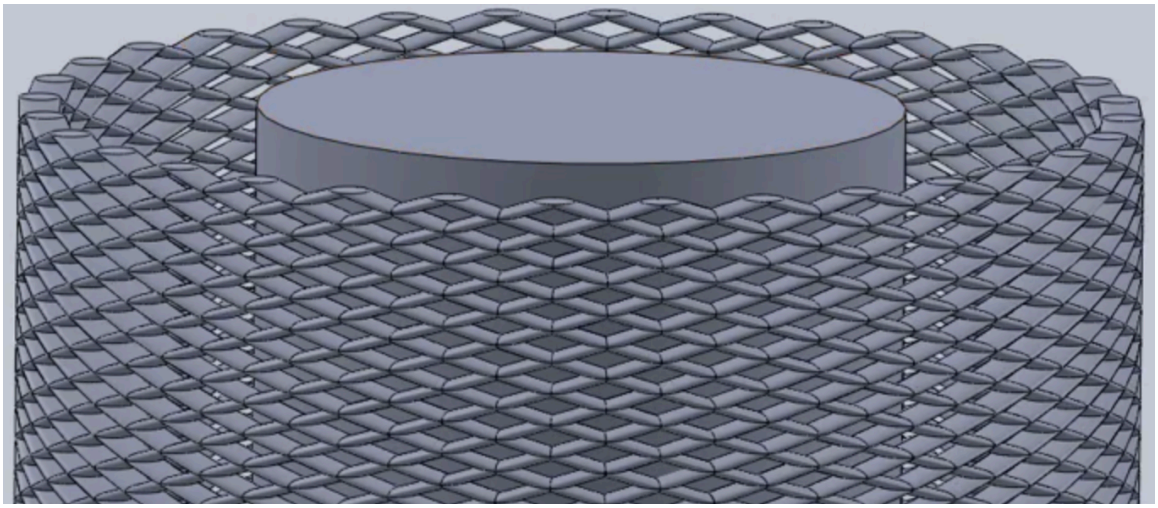

Figure 2.4. SolidWorks image of mesh cylinder designed via helical approach inner cylinder diameter is 6.35 mm.

The mesh cylindrical mold via the helical approach was conceived in response to several challenges that the solid outer cylinder presented regarding mass transfer and internal pressure buildup. The mesh design would provide an increased surface area which would bode better, in theory, for mass transfer.[15] This design was intended to be used with colloidal processing and pyrolysis.

2.1.4. Mesh Cylindrical-Alternative Approach

The procedure for constructing the base and circular sketch for the alternative approach was identical to that of the helical approach. At an arbitrary point along the circumference of the circle, a smaller circle of approximately 0.51 mm (0.02 inch) in

diameter was drawn and projected along the z-axis. Using the reference geometry feature, a one-line axis line of revolution was established at the origin that allowed for a separate cylinder to interconnect with the recently projected z-axis cylinder. Using the circular pattern feature for the cylinder projecting along the z-axis and the “linear pattern” feature for the revolving cylinder, multiple copies of each were made until the mesh outer cylinder was fully developed. Finally, a solid 6.35 mm diameter cylinder was constructed in the center by initiating and extruding on the positive z-face of the base. The complete design is given in Figure 2.5.

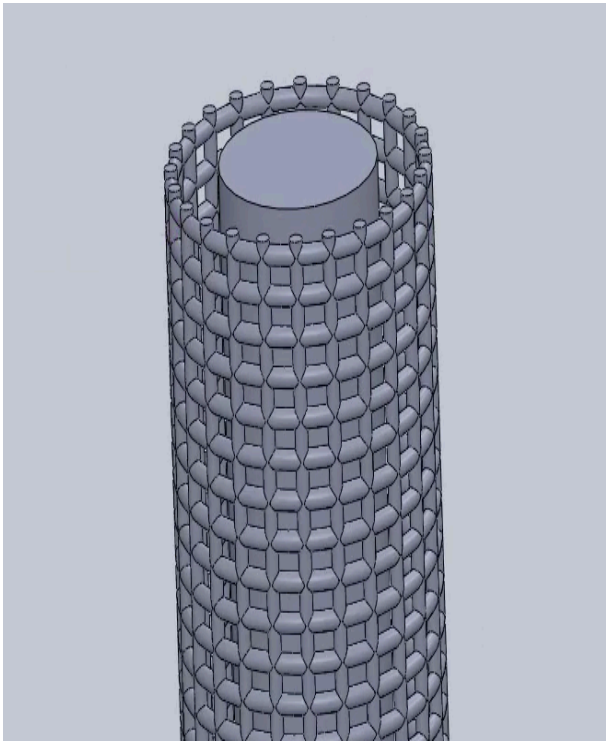

Figure 2.5. SolidWorks image of mesh cylinder designed via alternative approach. The outer diameter of the outer inncer cylinder 9.65 mm. The outer diameter of the inner rod is 6.35 mm. The area of the holes is 1.52 mm.

The mesh cylinder via the alternative approach was conceived in response to inconsistent printing of the mesh cylinder via the helical approach. It was believed that

lack of upward curvature would result in more consistent printing. This design was intended to be used with pyrolysis and colloidal processing.

2.2. SLA

This section will detail the printing of the aforementioned designs with SLA. Printing orientation, support, and printing success will be provided for each design.

SLA is a technique that implements a UV laser to trace and cure a photosensitive liquid resin to obtain the desired design. SLA is advantageous because it yields smooth surfaces and high resolution of small intricate details.[9] Such a quality is crucial for the aforementioned molds that have small holes.

To print the aforementioned designs, a Formlabs 2 printer was used. An image of the Form 2 is provided in Figure 2.6.

Figure 2.6. An image of the Form2, which has a build volume of 145x145x175mm. It is Formlabs' second-generation desktop printer and was used to print the designs presented in this study.[16]

The Form 2 employs a bottom-up orientation. The bottom-up orientation has a transparent bottom surface that allows the light of the laser to pass through and cure a

cross-section along the design path, but it prevents the cured resin from sticking to the surface. The resin is detached from the bottom of the tank and moves up with the build platform. The Form 2 produces the desired design by repeatedly UV curing and detaching from the bottom surface layer-by-layer until the object is complete.

The Form 2 comes with a companion program, PreForm. In Preform, the design .STL file is imported, and the orientation, support, and layer thickness are set. Most of the standard resins are capable of layer thicknesses of 25, 50, and 100 microns. Selecting the appropriate layer thickness is dependent upon design features and the resin used, as there is a tradeoff between time and improved accuracy. Therefore, as a general rule, a layer thickness of 25 microns is reserved for capturing designs with intricate features.[17]

2.2.1. Printing of Movable Mold

In Preform, the inner and outer cylinder designs were oriented vertically with auto-generated mini-supports at the bases. Formlabs' High-Temperature resin was used to print both designs concurrently. There were 178 layers that printed over 1.25 hours. The prints were subsequently washed in an Isopropyl (IPA) bath for 5 minutes and placed in a curing oven at 80 °C for 120 minutes.

The fins on the top of the outer cylinder presented a challenge as they were overhangs, which are extended unsupported features. Nevertheless, the majority of the fins did successfully print, but the thinness of these features resulted in fragility. In fact, a portion of one of the fins broke, as shown in Figure 2.7.

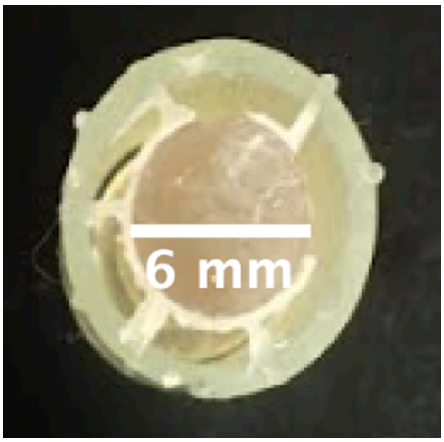

Figure 2.7. Finished movable mold after printing with Formlabs standard High-Temperature V2 resin and post-processing. The outer and inner cylinder are shown together to demonstrate how the mold will be used.

This compromised the parts ability to be reused and, therefore, the resulting ceramic's reproducibility. The inner cylinder printed without issue which may also be seen in Figure 2.7

2.2.2. Printing of The Solid Cylindrical Mold

Printing of the solid cylindrical mold was straightforward. In PreForm, the design was oriented vertically with auto-generated mini-supports at the base. A layer thickness of 100 microns was selected because there were no intricate details. Formlabs' High-Temperature resin was used to print 328 layers over 5.75 hours. The print was subsequently washed in an IPA bath for 5 minutes and placed in a curing oven at 80 °C for 120 minutes. The final parts were printed accurately with well-defined smooth surfaces as shown in Figure 2.8.

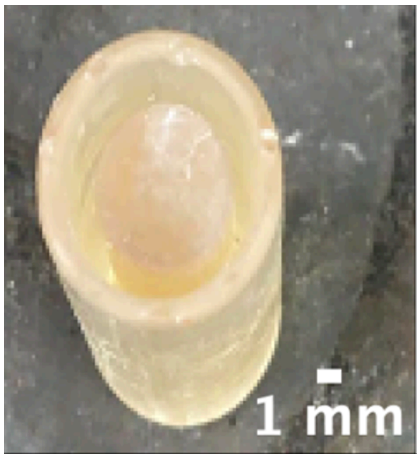

Figure 2.8. Finished solid cylindrical mold after printing with Formlabs standard High-Temperature V2 resin and post-processing. The solid cylindrical mold was printed with high accuracy and smooth finishes.

2.2.3. Printing of Mesh Cylindrical Mold-Helical Approach

In PreForm, the mesh mold via the helical approach was oriented vertically with auto-generated mini-supports at the base. A layer thickness of 25 microns was selected so that the printer would capture the small holes of the design. Formlabs' High-Temperature resin was used to print 328 layers over 1.75 hours. It was subsequently washed in an IPA water bath for 5 minutes and placed in a curing oven at 80 °C for 120 minutes.

Printing the mesh mold designed via the helical approach was complicated by the presence and shape of the small holes in the outer cylinder. This was further exacerbated by the upward curvature of the interconnecting shapes. This combination of design flaws resulted in overhangs. Figure 2.9 shows that this manifested in poorly defined holes or complete hole closure.

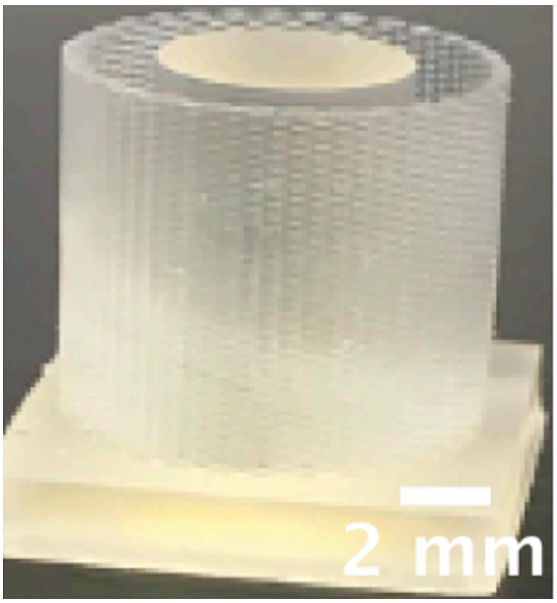

Figure 2.9. Finished Mesh Mold via Helical Approach after printing with Formlabs standard High-Temperature V2 resin and post-processing. Considerable hole closure was observed.

The inaccuracies in printing were the result of drooping, which is when layers spill onto other lower layers prior to hardening.[18] One way to combat this is to add support structures to the overhangs. [18]However, given the size and number of holes, additional supports led to an overly complex design in PreForm with virtually no improvement in printing success.

2.2.4. Printing of Mesh Cylindrical Mold-Alternative Approach

In PreForm, the mesh mold via the alternative approach was oriented vertically with auto-generated mini-supports at the base. Formlabs' High-Temperature, Draft, and Clear resins were used. Of these resins, the Clear displayed the best printing performance and will be discussed hereafter; both High-Temperature and Draft resins suffered from hole closure. After selecting a layer thickness of 25 microns, Formlabs' Clear resin was used to print 1199 layers over the course of 5.25 hours. It was subsequently washed in an IPA bath for 10 minutes and placed in a curing oven at 60 °C for 15 minutes.

Although the mesh mold via the alternative approach was susceptible to hole closure, a significant improvement over the helical approach was observed. Molds printed with clear resin exhibited no hole closure as Figure 2.10 demonstrates.

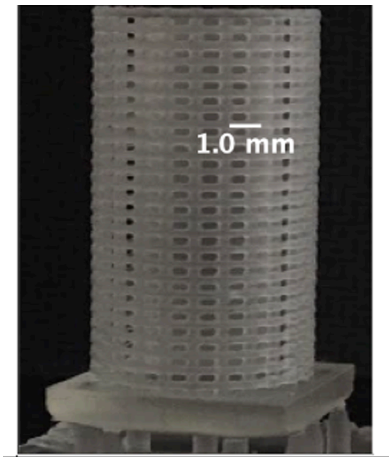

Figure 2.10. Finished Mesh Mold via Alternative Approach after printing with Formlabs standard Clear V2 resin and post-processing. Virtually no hole closure was observed.

The improved printing performance may be attributed to the design's ability to support itself coupled with the Clear resin curing faster than other resin types under UV light.[13,18]

2.3. Analysis Of Casting Techniques

This section will discuss the efficacy of the molds in producing alumina supports when coupled with conventional techniques, thereby addressing objective 3.

It must also be noted that the intimate details of the procedures for these techniques will be omitted in this section and discussed in greater detail in chapter 4 if relevant. This section seeks to present how these techniques helped to guide the decision-making on selecting a design for continued exploration rather than providing a final methodology.

2.3.1. Colloidal Processing with Movable Mold

The slurry with the composition presented in Table 2.1 was used to cast and asses mold viability.

Table 2.1. Composition of slurry used in initial exploration of molds.

Compound	Weight Percentage (%)
Alumina	56
Polysulfone(PS)	7
PVP K30	2
N-Methyl-2-pyrrolidone (NMP)	35

The slurry was loaded into a syringe and placed at the base of the mold, and a force was applied to the syringe plunger. This loading process proceeded until the slurry filled the annular cavity of the mold. Once the load was complete, a force was applied to the base of the inner cylinder to push it through the outer cylinder into a DI water bath. The resulting structures after several trials are presented in Figure 2.11.

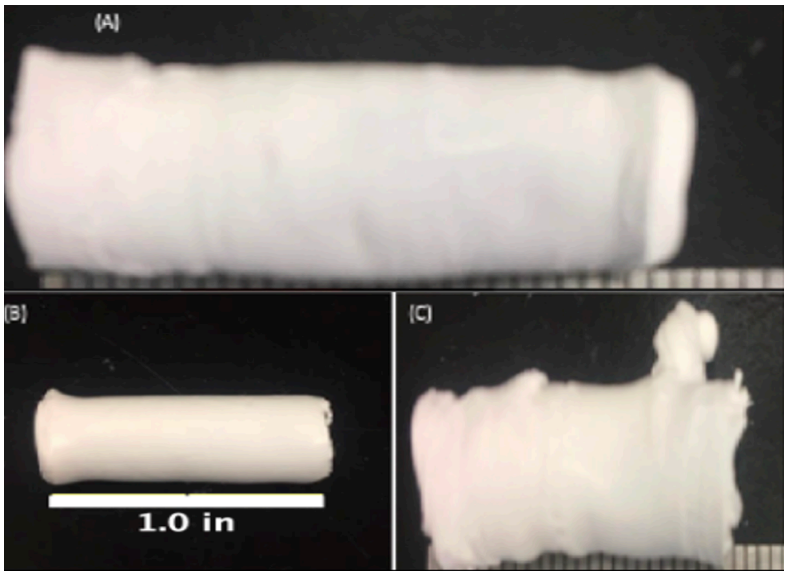

Figure 2.11. Three separate trials of colloidal processing with the movable mold. (A) Green body is slightly longer than desired.(B) Most accurate green body of the trial. However, right end is thinner. (C) Green body was severely deformed.

Figure 2.11 (B) demonstrates that the movable mold could yield a usable green body. However, Figure 2.11(A) and Figure 2.11(C) indicate that the movable mold was not able to do this consistently. In addition, all three green bodies were thinner than desired as they did not assume the thickness of the mold. This thinness may be attributed to very quick demixing as both the inner and outer surfaces were exposed to water simultaneously.[19]

2.3.2. Colloidal Processing with Solid Cylindrical Mold

The solid cylindrical mold's loading process was identical to the procedure presented in section 2.3.1 Once the mold was filled, the mold and the slurry were immersed in a DI water bath for approximately 48 hours. The immersion in water was to solidify the slurry and form the membrane matrix. After the mold was removed from the DI water bath, the procedure stalled as the substrate could not be demolded. The outer cylinder of the mold could not be removed from the membrane without potentially damaging the membrane.

In an effort to isolate and retain the alumina substrate, the mold/substrate composite was sintered with the hope that the membrane would maintain its structure. After sintering, it was observed that the membrane had collapsed, failing to retain the shape of the mold. The mold was believed to have collapsed before the alumina particles could sinter together. This theory was further validated by a Thermogravimetric Analysis (TGA) experiment on the High-Temperature mold with a Shimadzu TGA-50, incrementing temperature 5°C/min under 50ml/min airflow.

The TGA experiment determined that over 87.5% of the mold had decomposed by 450° C, which constitutes a significant gap from the onset of alumina sintering, typically between 1100 °C to 1700 °C.[20–22] Thus, a technique that would enable the mold to retain its shape well beyond this decomposition range was desired.

2.3.3. Pyrolysis

According to multiple studies, shape retention for the mold beyond the decomposition range specified in 2.3.2 was, in fact, possible.[15,23] When placed in an inert environment with constant gas flow, the molds should convert to a sp^2-rich form known as glassy carbon. [15,23] The prevailing logic was that if the mold was able to retain its shape up to onset sintering temperatures, an alumina support could be fabricated. However, many of these studies cited a 75% to 80% reduction in size so original designs would have to be scaled up quite significantly.

A preliminary experiment was conducted with the solid cylindrical mold without scaling up for anticipated shrinkage. The mold was placed in a tube furnace, where it was subjected to 200 ml/min of Ar flow. With a ramp rate of 2 °C/min, the tube furnace temperature was raised to 600 °C and held for two hours. Then, with a ramp rate of 5 °C/min, the temperature was increased to 1000 °C, held for two hours, and subsequently cooled. After completion of this profile and examination of the remaining material, it was clear from the dark black color that conversion to glassy carbon had occurred, but the mold had failed to retain its shape, as shown in Figure 2.12.

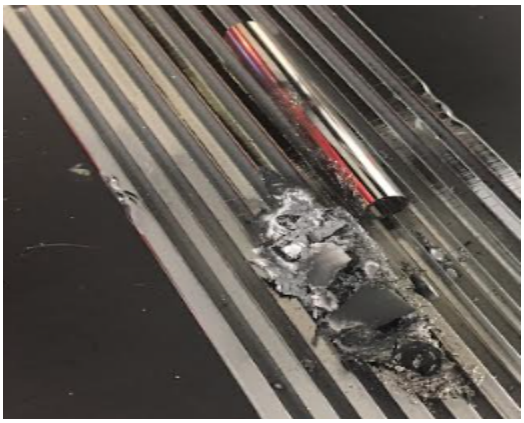

Figure 2.12. Image of solid cylindrical mold after completing sintering profile while subjected to 200ml/min Ar flow. The solid cylindrical mold converted to glassy carbon but did not retain shape.

The failure of the mold to retain its shape was the result of an inherently flawed design for pyrolysis. The solid bulky design impeded the degassing of the mold, which lead to high internal pressures and the subsequent collapse of the structure.[15] It was determined that a mesh structure with a higher surface area would allow for gas exodus without impinging upon the mold structure.

2.3.4. Colloidal Processing with Mesh Structure via Alternative Approach

Although the mesh structure was initially conceived to be compatible with the pyrolysis process, practical limitations prevented continued exploration. The preliminary experiment left a large amount of residual carbon material on the stainless-steel connections of the tube furnace. Even with a mesh structure, continued trial-and-error experimentation would have likely led to permanent damage and premature replacement of the stainless-steel piping. Thus, there was an incentive to revisit colloidal processing with the newly fabricated mesh structure.

The procedure proceeds as it did in section 2.3.2. One difference in procedure when compared to that of the solid cylindrical mold was that the mesh cylindrical mold was wrapped in Teflon tape to cover the holes of the outer cylinder. The wrapping helped to hinder the slurry material from escaping the annulus when loading. After removing the mold and membrane composite from the water and allowing adequate time to dry, a fully isolated alumina green body, as shown in Figure 2.13, was obtained by mechanically demolding.

Figure 2.13. Isolated alumina green body after completing phase-inversion via immersion precipitation and demolding.

This was one of the true advantages of casting with the mesh cylindrical mold compared to the other molds; the thin features of the outer cylinder made isolating the alumina membrane feasible. Despite this progress, the alumina support still collapsed upon sintering. The cause of the collapse was traced back to immersion precipitation, as shown in Figure 2.14

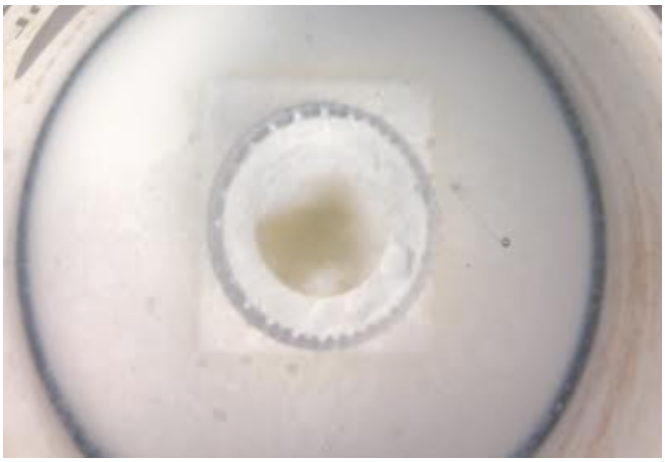

Figure 2.14. Image of mold/slurry composite immersed in DI water while slurry undergoes phase-inversion to form membrane. The surrounding white material is alumina that has leached from the slurry.

Figure 2.14 shows a large amount of white material surrounding the mold. It was hypothesized that this was alumina leaching from the slurry during phase inversion. A TGA experiment was performed to verify this hypothesis. In the TGA experiment, a pre-sintered hollow fiber of the same composition known to undergo successful sintering was provided by a colleague and used for comparison. The data for this TGA experiment is provided below in Figure 2.15.

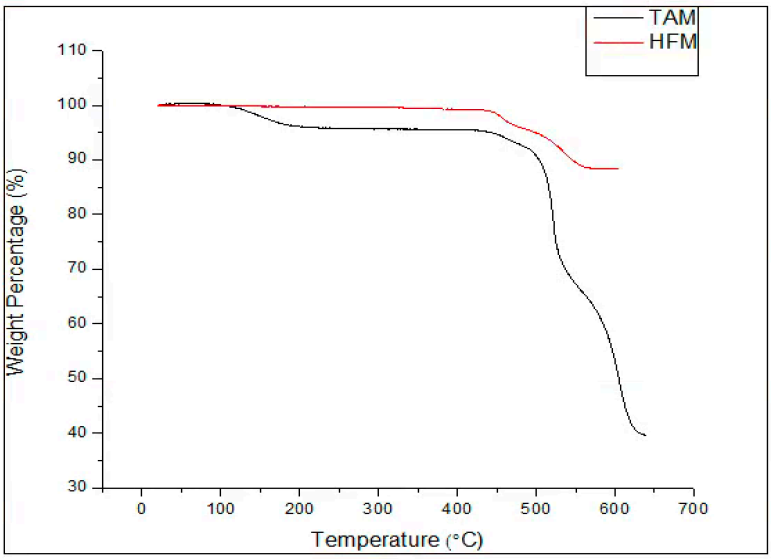

Figure 2.15. TGA data comparing tubular and hollow fiber green bodies. TAM refers to the tubular alumina membrane that experienced leaching. HFM refers to the hollow fiber membrane known to undergo successful sintering.

The TGA data in Figure 2.15 confirmed that alumina was, in fact, leaching from the slurry. Although debinding temperature depends on the ceramic and binder being used, generally most of the organic material has decomposed by 600 °C.[24] After 600 °C, the weight percentage primarily refers to the ceramic material remaining in the sample. Therefore, the data in Figure 2.15 implies that only 40% of the original tubular alumina membrane sample was alumina. Juxtaposing this with the hollow fiber membrane, whose alumina concentration in the sample was 88%, it was clear that this little alumina was not enough to maintain its structure during sintering, hence the collapse. Despite the collapse, the results from colloidal processing with the mesh cylindrical mold via the alternative approach were auspicious as the focus shifted from designing a viable mold to tailoring the slurry composition to obtain an alumina support with the mesh cylindrical mold via alternative approach.

2.4. Selection

This section will explicitly state why the mesh cylindrical mold via the alternative approach was selected to fabricate alumina membranes and why other molds were eliminated from further exploration. Additionally, it will discuss why colloidal processing was selected as the technique to couple with the mesh cylindrical mold via the alternative approach.

2.4.1. Movable Mold

Although the movable mold was able to produce alumina green bodies, there were significant differences in structure between the green bodies. In addition to the disparities between green bodies, there were significant differences between the green bodies and the intended design; the green bodies were much thinner than intended. Moreover, the printing of the movable mold was not entirely successful as part of the fins were damaged, which impugned the design's printing consistency. Thus, a lack of reproducibility and accuracy in regard to casting and printing led to the exclusion of the movable mold.

2.4.2. Solid Cylindrical Mold

The solid cylindrical mold was eliminated because it was difficult to demold, and the solid outer cylinder hindered mass transfer. Once the slurry was loaded in the annular region of the mold, there was no approach to detach the mold from the membrane without damaging the membrane. Even with an alternative approach such as pyrolysis, the solid bulky structure collapsed due to an internal pressure buildup.

2.4.3. Mesh Cylinder via Helical Approach

As discussed in section 2.2.3, the mesh cylinder via the helical approach was difficult to print successfully as hole closure typically occurred. The inability to print well-defined holes precluded its exploration with colloidal processing. Additionally, it was far more challenging to control hole size via the helical approach than the alternative method. Thus, even if the hole closure was the result of the High-Temperature resin rather than an inherently flawed design, the lack of tunability forced this design to be excluded.

2.4.4. Mesh Cylinder Via Alternative Approach

The mesh cylinder via the alternative approach offered a number of advantages over the other designs. The holes on the outer cylinder allowed for radial mass transfer through direct contact with the coagulation bath. Furthermore, because of their thinness, the struts on the outer cylinder were easily broken, allowing the alumina support to be released. Ultimately, these advantages culminated in a design that could potentially fabricate supports with high accuracy, repeatability, and reproducibility. The final dimensions for the mesh cylinder via alternative approach are provided in Table 2.2.

Table 2.2. Final Dimensions for Mesh Cylinder via Alternative Approach

Dimension	Value (mm)
Outer Diameter	9.65
Inner Diameter	6.35
Volume	1.05 (mL)
Diameter of Interconnecting Cylinders	0.51
Annulus Thickness	1.65
Area of Holes	1.52
Length	25.4

Colloidal processing was selected as the technique to fabricate alumina substrates because of its ease of operation, expected reproducibility, and scalability. Pyrolysis was not considered because it was damaging to the equipment. Furthermore, pyrolysis was prohibitive in that molds would need to be five times larger to achieve the desired final dimensions.

2.5. Conclusions

This chapter demonstrated that the Form 2 was capable of printing the mesh cylindrical mold via the alternative approach with high accuracy consistently. Although it was susceptible to hole closure, its superior design allowed it to self-support. This allowed the mesh cylindrical mold via the alternative approach to outperform other designs during preliminary fabrication testing. Thus, it was concluded that the mesh cylindrical mold via the alternative approach would provide the best chance to fabricate an alumina substrate after optimizing the procedure.

Chapter 3: Fabrication of Alumina Substrate (Support)

3.1. Introduction

In this chapter, the mesh cylinder via alternative approach (simply "mesh cylinder" hereafter) was identified as a mold with which a cast slurry could be solidified and eventually isolated in the shape of the mold. However, it was also observed that a robust alumina membrane was not yet attainable as the green body would collapse upon sintering. This chapter builds on these observations and presents how various aspects of the preliminary procedure were manipulated and optimized until an alumina membrane was obtainable consistently. Once the repeatable procedure has been presented, discussion will proceed to characterization of the alumina membranes. From this characterization, the impact of 3D printing on attaining membranes with similar morphological properties will be assessed.

The fabrication procedure is decomposed into 5 major steps: slurry development, loading, phase-inversion/solve extraction, demolding and sintering. The content will be presented within an iterative framework to highlight that final methodology is consistent with objective 4. The advantage of this strategy is that the evolution from preliminary methods and accompanying rationale is easily discernable. The properties of the final alumina substrates were measured and discussed. They will illuminate various relationships with solid loading, sintering holding time, and sintering temperature.

3.2. Materials

N-Methyl-2-pyrrolidone (NMP), Polysulfone(PS, average Molecular weight (Mw) ~ 35,000), and Polyvinylpyrrolidone (PVP, average Mw~ 40,000) were purchased from Sigma Aldrich. Anhydrous ethanol was purchased from Pharmco. Polyvinyl Butyral

(PVB, B-98, Mw 40,000-70,000) was purchased from Acros Organics. Alumina (Al_2O_3) was purchased from Alfa Aesar with an average particle size between 0.25 and 0.35 microns.

3.3. Alumina substrate development

3.3.1. Slurry Development

This section will discuss why an NMP/Alumina/PVB system was chosen as the casting slurry and how the final composition was determined.

For all intents and purposes, mixing for the following systems was the same. The organic components were mixed at 60 rpm for at least 8 hours on a VWR magnetic stirrer. The necessary alumina powder was then added incrementally to the organic solution and allowed to mix for 48 hours, at which point a uniform slurry was typically obtained.

(A) NMP/PS/PVP/Alumina: In the first system explored, NMP, PS, and PVP functioned as the solvent, binder, additive, respectively. This system is commonly used to fabricate alumina hollow fibers.[25,26]NMP is commonly used as a solvent due to its polar nature, relatively high boiling point, and its wide range of solvency for inorganic and organic compounds.[27]Polysulfone is known for its stability, high mechanical strength, and ease of modification.[28] PVP is used as a pore-former that increases the hydrophilic character and viscosity of the doping system, which typically results in a structure with finger-like pores.[29,30] The weight percentages for this slurry are provided in Table 2.1.

As communicated in Chapter 2, this combination of components was unsuccessful with the mesh cylinder; however, the slurry was successful with the movable mold with respect to obtaining a sinterable green body. Together, these

observations indicated that this slurry was capable of yielding a tubular membrane when all surfaces were in simultaneous contact with the non-solvent phase. Otherwise, polysulfone was not capable of sufficiently entrapping the alumina particles into the membrane matrix. Although the mechanism is not entirely understood, one possible explanation considered the interaction between polysulfone and alumina.

Generally, polymer binding proceeds through physical or functional group interaction.[31] Of the two binding mechanisms, physical interaction or physisorption typically leads to weaker interactions. Polysulfone likely adsorbed to alumina through physisorption, and its weak interaction was overcome by alumina's affinity for water.[32,33] This resulted in a leaching rate greater than the precipitation front rate, hence the alumina accumulation in the water bath. [34]The slurry's inability to yield a membrane that satisfied the established criteria necessitated a new slurry composition.

(B) Ethanol/Polyvinyl Butyral (PVB)/Alumina: In this system, ethanol and PVB operated as the solvent and binder, respectively. When ethanol and PVB are mixed in solution with a ceramic phase, it is typically done for tape casing applications.[35]Ethanol is commonly used as a solvent because it is inexpensive, volatile, non-toxic, and amphipathic, which makes it a compatible solvent for many compounds.[36] PVB is used as a binder because of its strength, solubility, and tunable glass transition temperature.[35,37]

The slurry composition explored for this system is provided in Table 3.1.

Table 3.1. Composition of Ethanol/PVB/Alumina system given in weight percentages.

Compound	Weight Percentage (%)
Alumina	50
Ethanol	43.75
PVB	6.25

The major difference between the PVB-based system and the PS-based system was the performance during phase inversion. The PVB-based slurry greatly improved alumina retention within the slurry. There was virtually no alumina accumulation in the coagulation bath. The improved retention may be explained through a portion of the chemical structure of PVB in Figure 3.1

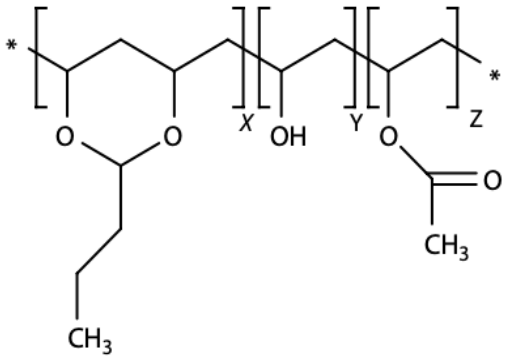

Figure 3.1. Terpolymer structure of PVB. Image is adapted from ref 38.

The terpolymer structure in PVB is the result of incomplete conversion of PVA and products remaining linked in the polymer chain during the fabrication process.[38] This structure contains a carbonyl group and a hydroxyl group that chemically interact with the surface of alumina.[39] The result is a strong bond that is able to tightly hold alumina in the membrane matrix during phase inversion.

Although the slurry was able to successfully entrap the alumina particles, it did suffer from an incomplete filling of the mold, also known as short shots. It was difficult to pinpoint what caused the short shots as there were a number of potential reasons, but they were likely a result of ethanol's volatility, which had a twofold effect: quick drying and susceptibility to air bubbles.[40] Quick drying resulted in partial solidification of sublayers which in turn resulted in weak bonding between successive layers.[40] The presence of air bubbles restricted the flow of the slurry. Thus, a solvent that would not suffer from these shortcomings was desired.

(C) NMP/PVB/Alumina: NMP was substituted for ethanol to confirm if the incomplete filling of the mold was in fact attributed to ethanol's volatility. In theory, NMP should prevent quick drying as it is far less volatile than ethanol. Initial NMP composition was maintained at 43.75% so adequate comparisons between NMP and ethanol could be drawn. The complete slurry composition is provided Table 3.2.

Table 3.2 Composition of NMP/PVB/Alumina system given in weight percentages

Compound	Weight Percentage (%)
Alumina	50.0
NMP	43.75
PVB	6.25

The doping solution with NMP exhibited improved mold filling. The final sintered membrane retained the mold design with greater accuracy, as shown in Figure 3.2.

Figure 3.2. Alumina membrane green body from NMP/PVB/Alumina slurry. The slurry resulted in better filling which in turn led to better shape retention of the mold. However, there are large holes, surface defects, and slight tilt.

Implementing NMP as the solvent led to significant improvement and established that this combination of components could yield a membrane with the intended design. However, large macroscopic holes portended a weak unsatisfactory microstructure with pinholes and defects. Thus, the focus shifted to tailoring the alumina weight percentage to limit the presence of these impediments.

(D) Slurry Rheology: The weight percentage of alumina, at a fixed ceramic to binder ratio of 8, was varied from 50% to 60%, incrementing by 5%. The solid loading was fixed to this range because mixing above 60% was not feasible and below 50% would yield undesirable mechanical properties. A ceramic to binder ratio of 8 was selected to obtain smaller pores.[25] A HAAKE MARS iQ Rotational Rheometer with air bearing characterized the flow behavior of the slurries at different alumina weight fractions. Characterizing the flow provided insight and guidance as to what solid loading would yield the most desirable membrane.

Stress-controlled and strain-controlled experiments were run on the different compositions. Slurries with a solid loading of 50% and 55% exhibited Newtonian flow;

whereas, slurries with a solid loading of 60% exhibited shear-thinning flow. Stress-controlled and strain-controlled experiments for a solid loading of 60% are displayed in Figure 3.3

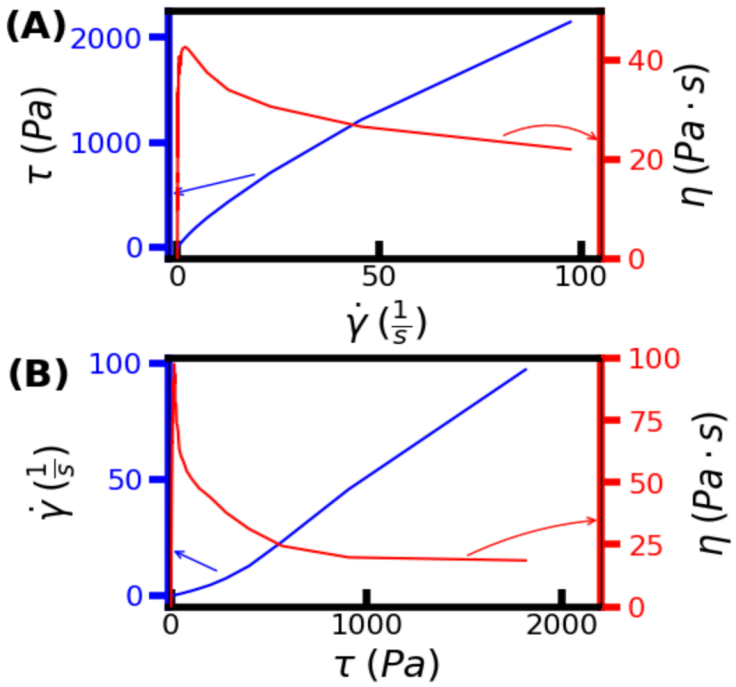

Figure 3.3. Rheological data for slurries with alumina weight fraction of 0.60.(A) Shear-controlled data with viscosity and stress as response variables. (B) Stress-controlled data with viscosity and shear rate as outputs. Both plots indicate shear-thinning behavior.

The shear-thinning behavior observed in Figure 3.3 is desired in casting or mold applications because it allows the slurry to flow under the high shear rate conditions in the syringe but remain fixed in the mold under low shear rates.[41] The shear-thinning behavior at 0.60 alumina loading helped to improve the filling of the mold and mitigate the presence of holes and short shots.

3.3.2. Slurry Loading

Before loading, the slurry was degassed for 10 minutes under vacuum with an Isotemp Vaccum Oven (Model 280A). A degassing time of 10 minutes was decided upon

after performing preliminary experiments at 10 minutes, 20 minutes, and 30 minutes. Higher degassing times led to slurry drying, so they were rejected in favor of 10 minutes. Degassing the slurry helped to eliminate air bubbles that could result in large pores and compromise the final ceramic structure.[41]

After degassing the slurry, the inner cylinder was lubricated. Lubrication was a critical step as it allowed for separation of the alumina membrane from the mold without compromising membrane structure. Preliminary fabrication procedures did not include a lubrication step, resulting in membrane distortion due to mechanical pulling (Figure 2.13). Lubrication of the mold resulted in a reduction in friction between the inner cylinder and alumina substrate. The lubricant creates a fluid film so the two surfaces are not in direct contact with each other as shown in Figure 3.4.

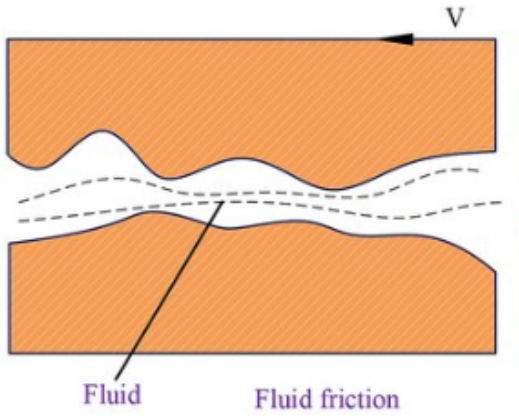

Figure 3.4. Schematic demonstrating the effect of adding a lubricant on the interaction between two solid surfaces. Adapted from ref. 42

With a pipette, Super Lube silicone oil was used to lather the inner surface of the mold. Silicone oil was selected as the lubricant because its low surface tension (0.02 J/m^2) allows it to wet most surfaces.[43] Furthermore, its viscosity was sufficiently high

enough to produce a thick enough film to readily pull the alumina membrane off the mold.

The outer cylinder of the mold was wrapped tightly with Teflon tape. The mass of the mold with Teflon tape was obtained. Then, a disposable 1 ml Luer-slip syringe was loaded with the degassed slurry. A 22-gauge, 38.1 mm long needle with a beveled tip was attached to the syringe and placed at the base of the mold. A force was applied to the syringe plunger until the slurry filled the mold cavity. The mold was intermittently tapped during the filling to prevent the slurry from mounding and ensure uniformity. After the annulus was filled with slurry, the mass of the mold with the slurry was obtained. The slurry amount added to the mold was determined with the masses before and after loading. This measurement procedure was done in lieu of tracking the volume in the syringe to avoid incorrect measurements due to dead volume.

3.3.3. Phase-Inversion/Solvent Extraction Via Immersion Precipitation

After loading the mold, the Teflon tape was removed and the mold/slurry composite was immersed in a DI water bath. Water, as a non-solvent for PVB, initiated a state of thermodynamic instability for the slurry. It was then energetically favorable for the slurry to undergo what is known as “bindoal demixing.” During bindoal demixing, the slurry separated into a polymer-rich phase and a polymer-lean phase where the polymer-rich phase formed the membrane matrix, and the polymer-lean phase formed the pores of the membrane.[34,44] A simplified ternary phase diagram depicting the pathway is offered in Figure 3.5.

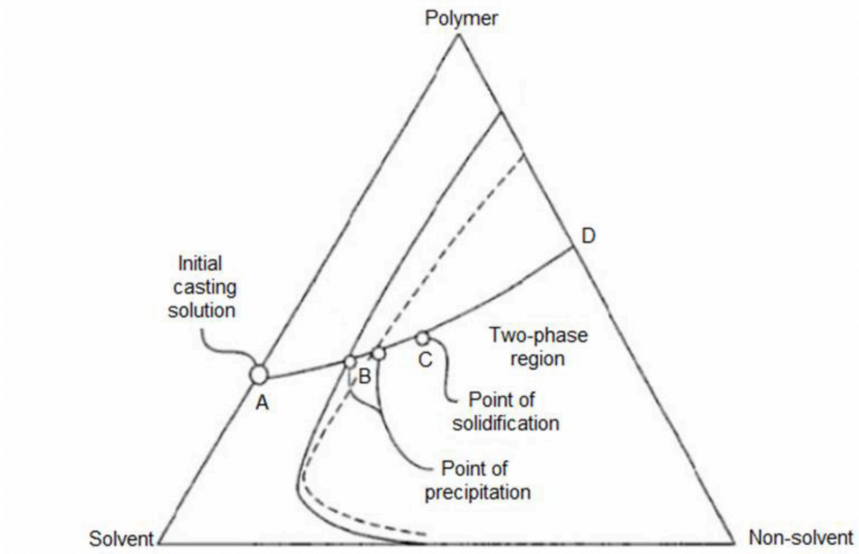

Figure 3.5. Ternary phase diagram of polymer, solvent, non-solvent with a representative pathway of binodal demxing. Adapted from ref 45

In Figure 3.5, point B corresponds to an arbitrary point where the composition lay on the bindoal. At this point, nuclei originated, and the slurry demixed into the two phases. The polymer-rich phase was still liquid, but the continued counter-diffusion of the solvent and non-solvent led to the solidification of the polymer-rich phase at point C. After this point, diffusion slowed until point D was reached.

The kinetics of the phase inversion process are also critical as they dictate the morphology of the resulting structure. It is believed that "instantaneous demixing," which is characterized by the rapid exchange of solvent and non-solvent, results in the formation of finger-like or tear-like macrovoids. [26,34,46–48]Conversely, "delayed demixing," which is characterized by pore formation after a sufficiently long time, results in a denser sponge-like structure. [26,34,46,47,49] However, the demarcation between instantaneous and delayed demixing is not well-defined in literature and must be determined empirically case-by-case.[34,48]

3.3.4. Demolding

After 24 hours of immersion in the coagulation bath, the mold/substrate composite was removed and cut at the base using a blade. Cutting at the base was done to remove the substrate from the inner cylinder of the mold while keeping it attached to the outer cylinder. The substrate was allowed to dry for approximately 24 hours. After 24 hours, the outer cylinder was removed from the substrate by mechanically pulling at the struts. The demolding process was executed in this manner to minimize damage to the substrate.

After the samples were demolded, they were qualitatively analyzed. The analysis included describing the presence of holes, non-uniformities, cracks, and so forth. Each membrane was also assigned a unique ID (UID) and stored in a container until sintering.

3.3.5. Sintering

Before placing alumina tubes into the furnace, the lengths, inner diameters, and outer diameters were measured using a caliper with an intrinsic measurement error of 0.1 mm. Calipers ensured high accuracy and precision of dimensional measurements. Green body measurements were critical to determining dimensional shrinkage post-sintering.

After demolding and dimensional measurement, the alumina green body was sintered to yield the final dense alumina membrane. The alumina green body was subjected to the sintering profile in Figure 3.6

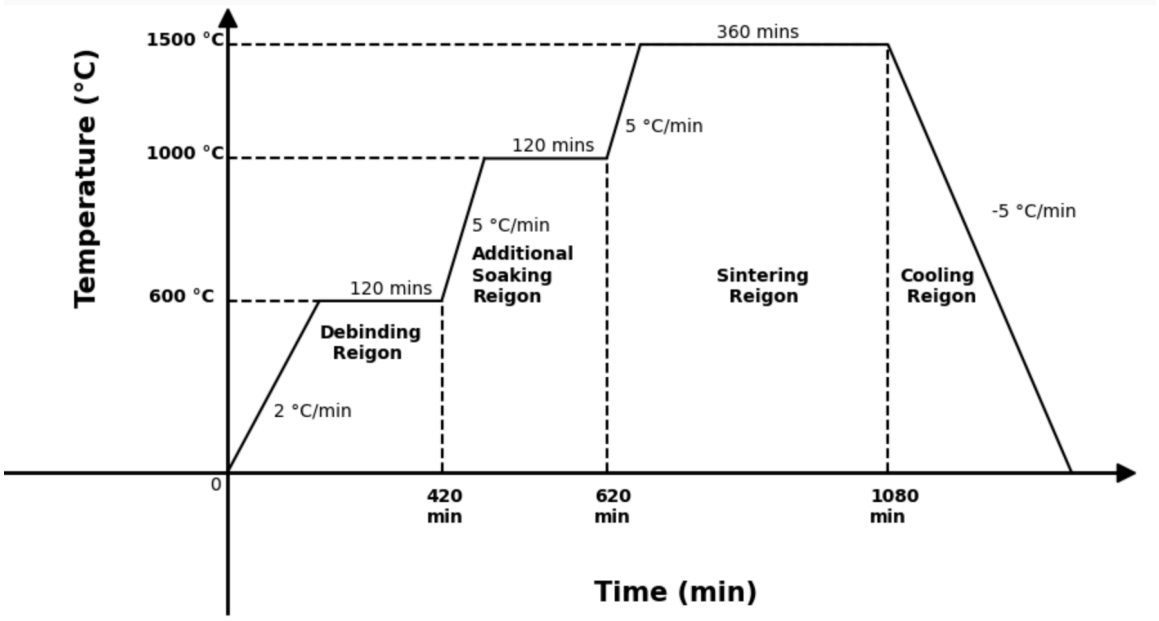

Figure 3.6. Sintering profile used to fabricate alumina membranes.

The temperature profile in Figure 3.6 was adapted from the preliminary trials with the NMP/PS/PVP/Alumina system. Although the NMP/PVB/Alumina system was significantly different, the temperature profile was suitable because most binders decompose at 600°C.[24] Furthermore, extant literature indicates that the majority of PVB decomposes by 440 °C, and this temperature may be depressed even more in PVB/alumina systems due to the catalytic character of alumina.[50,51] The holding time at 1000 °C was incorporated to enhance homogenization. Finally, the sintering temperature of 1500 °C was selected because it approached the upper limit of the sintering temperature range for alumina and, in theory, helped to maximize physical and structural properties.

The above sintering profile was varied to determine the effects of manipulating process parameters on alumina microstructure and physical properties. The two process parameters that were manipulated were sintering temperature and holding time. Holding

time varied from 6 hours, 8 hours, and 10 hours at a fixed temperature of 1500 °C. Sintering temperature was varied from 1500 °C, 1550 °C, and 1600 °C at a fixed holding time of 6 hours.

3.4. Properties of sintered alumina substrates

3.4.1. Macrostructure

This section will qualitatively describe the structure of the alumina supports. Characterizing sintered alumina parts was important because it allowed for intra-study comparison and inter-study comparison. The parts demonstrated a well-defined pattern on the outer surface, well-defined radial cross-sections, and were principally linear in the axial direction. In addition, they were not frail as they did not collapse upon touch and could be dropped without breaking. There were defects, but none of the defects were egregious enough to discard the support. Images of the sintered alumina supports are provided in Figure 3.7.

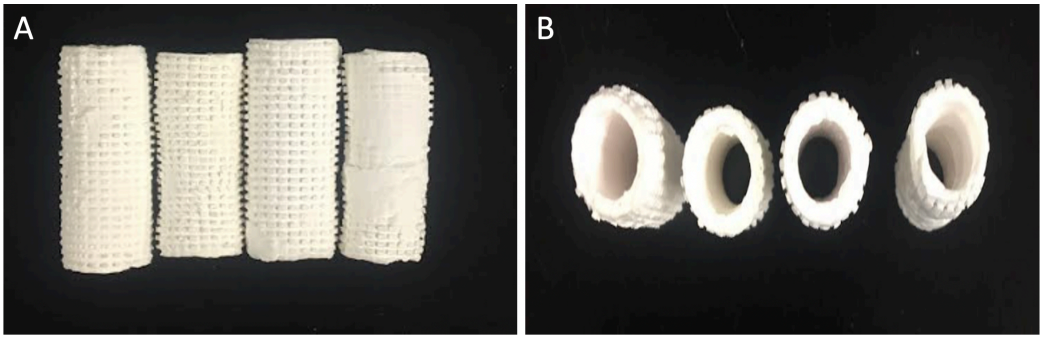

Figure 3.7 Images of Sintered Alumina Supports. (A) Similarities between sintered alumina supports lengthwise. (B) Similarities between sintered alumina supports radially.

The similarities between the sintered parts in Figure 3.7 support the notion that the procedure is repeatable. Loading and phase inversion via immersion precipitation are anisotropic processes that could have resulted in macroscopic disparities. Therefore,

although there are minor differences between the supports, it is clear that potential sources of macroscopic variability were properly mitigated in the fabrication procedure.

3.4.1.1. Changes with Height

The sintered alumina substrates were qualitatively characterized as height was varied. It was important to vary height as many applications will necessitate longer membranes. Thus, it was imperative to determine whether fabricating at increased heights was feasible and if structural integrity would be maintained as the height varied. Figure 3.8 provides an image of the three different heights together.

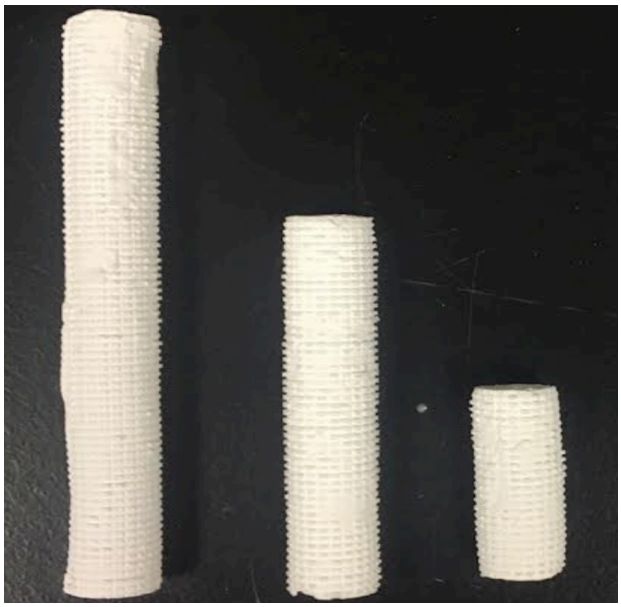

Figure 3.8 Sintered alumina supports at the three different heights (25.4 mm, 50.8 (2 in) mm, and 76.2 mm (3in)) explored.

The supports in Figure 3.8 illustrate that the procedure could be scaled-up to accommodate 50.8 mm and 76.2 mm parts. They showed a minimal loss in structural integrity as the longer parts also had well-defined outer surface patterns and were principally linear. However, the 76.2 mm support did suffer from a slight tilt due to

instability of mold's inner cylinder. The inner cylinder was unstable because it approached aspect ratio constraints at 76.2 mm.[16] Thus, although it was still principally linear, it was not as accurate as the smaller supports.

3.4.1.2. Digital Microscopy

Some of the samples were analyzed under digital microscopy. A Dino-Lite handheld digital microscope with adjustable magnification between 10x-90x was used to obtain high resolution macroscopic images. Images from digital microscopy with specimen UID 7 are provided in Figure 3.9

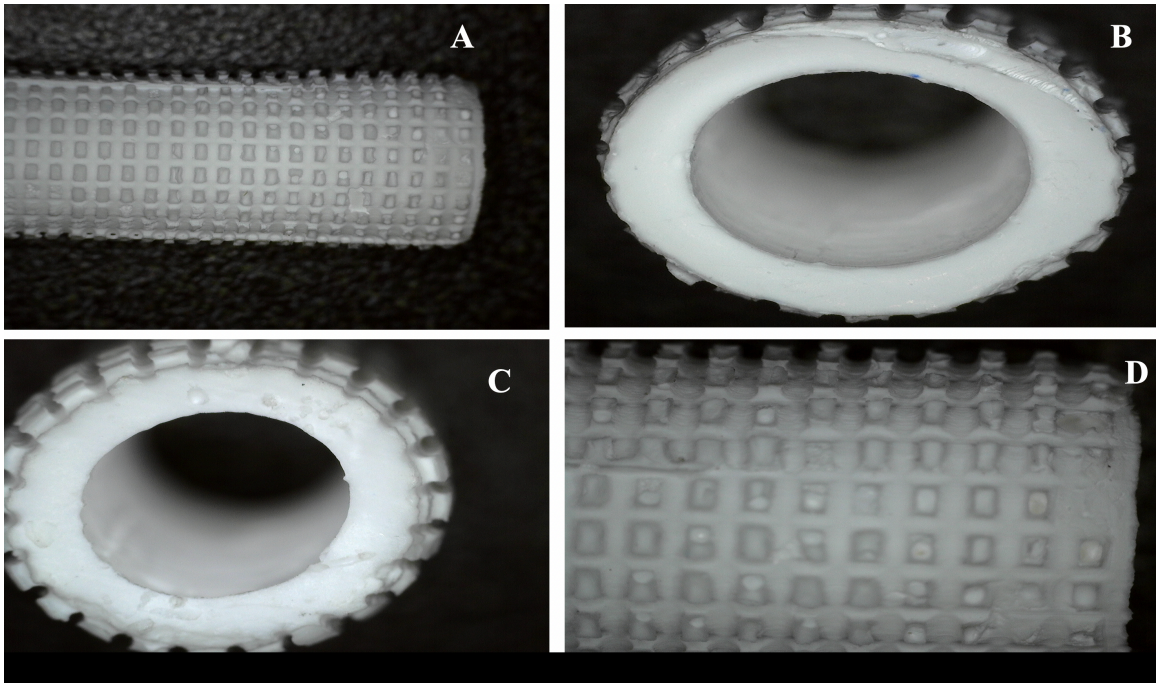

Figure 3.9 Images from digital microscopy for specimen UID 7. (A) Outer surface with highly ordered pattern. (B) Bottom radial cross-section. (C) Top radial cross-section. (D) Close-up of outer surface with highly ordered pattern.

Figure 3.9 displays how the elements of the mold design manifested into features on the final alumina support. For instance, Figure 3.9(A) and (D) show the highly ordered pattern on the outer surface resulting from mold design holes. The pattern provided the

support with a tangible roughness. Literature regarding the effect of surface roughness is dichotomous as some contend it increases mass flux, while others say it decreases mass flux.[52–54] In any case, it may be concluded that the effect of roughness is application-dependent which renders the alumina support all the more versatile given its smooth inner surface. The smoothness of the inner surface may be seen in Figure 3.9(C) and (D). Also in these images, the well-defined outer and inner diameters may also be seen. However, some minor inconsistencies were present as well. In Figure 3.9(B), the outer diameter was slightly damaged in the top right region, likely as a result of demolding. In Figure 3.9(C), the shape and size of the diameters deviate slightly from the base in Figure 3.9(B). Neither of these issues was especially prevalent in the population of samples and may be tabled as characteristics unique to specimen 7.

3.4.2. Dimensions

After removing alumina tubes from the furnace, the lengths, inner diameters, and outer diameters were measured using a caliper with an intrinsic measurement error of 0.1 mm. Calipers ensured high accuracy and precision of dimensional measurements. Sintered body measurements were critical to determining dimensional shrinkage post-sintering. Quantifying the degree of shrinkage was essential because it captured the deviation from the intended design. Equation (3.1) presents the equation for dimensional shrinkage.

$$\Delta X = \left|\frac{X_2 - X_1}{X_1}\right| * 100 \quad \textbf{(3.1)}$$

In equation (3.1), X_2 refers to the value of the dimension after sintering, and X_1 is the value of the dimension prior to sintering. The dimensional shrinkage values for the total population, irrespective of fabrication parameters, is provided in Table 3.3.

Table 3.3. Shrinkage values in the Axial, Radial Outer Diameter and Radial Inner Diameter directions for the entire population of samples.

Dimensional Shrinkage	Min (%)	Median (%)	Max (%)	Mean (%)	STD (%)
Axial	1.00	15.4	24.0	15.4	4.00
Radial (Outer)	6.25	16.3	23.3	15.9	4.26
Radial (Inner)	8.33	18.3	29.4	18.5	4.90

The average shrinkage values were below 20%, with averages ranging from 15.4% to 18.5 %. These values are slightly higher than other studies that fabricated alumina tubular membranes with around 10.0% shrinkage, but they were lower than other studies that employed SLA that reached shrinkage values as high as 60.8%.[55] However, these studies used different systems, which would also influence the degree of shrinkage. Furthermore, scaling up mold design to compensate for this shrinkage is not prohibitive and can be executed easily with a Form 2. Another intriguing result in Table 3.3 is that the inner diameter underwent the most significant amount of shrinkage with the highest values for min, median, max, and mean. This is an indication that the membranes did, in fact, develop an asymmetric structure. The inner diameter likely underwent delayed demixing, which resulted in a relatively dense layer with smaller pores. Smaller pores typically shrink faster, hence the increased shrinkage percentage for the inner surface.[56]

Error! Reference source not found. The relationships between the dimensions and solid loading, sintering temperature, and holding time were explored.

3.4.2.1. Effect of Solid Loading

Solid loading is known to have a pronounced effect on the degree of shrinkage in ceramic systems. Shrinkage is an accepted by-product of the fabrication procedure, but typically, it can be controlled by increasing the solid loading. Thus, it was critical to determine how the NMP/PVB/Alumina system would behave with increased alumina concentration. Figure 3.10 presents the nature of this relationship for this study.

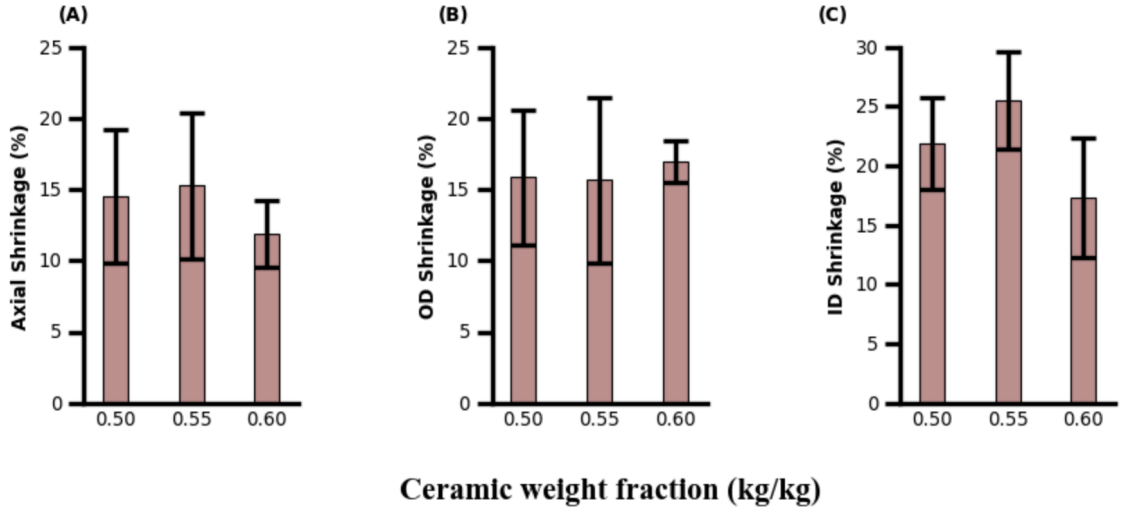

Figure 3.10. The effect of alumina weight fraction on dimensional shrinkage in the (A) axial direction, (B) radial direction for the outer diameter, and (C) radial direction for the inner diameter. Values provided are an average at a weight fraction

Figure 3.10 shows that for this system the relationship between solid loading and shrinkage was likely not linear, as a weight fraction of 0.55 was a locus of maximum shrinkage in two of the three dimensions and minimum shrinkage in the other. Assuming this observation was not the result of sample variability, this implies that the arrangement of particles at this solid loading was inefficient in the axial direction and on the inner

surface of the tube.[57] Conversely, a weight fraction of 0.60 represented a maximum in particle packing efficiency.[57] Interstitial pore space was minimized at this weight fraction, resulting in reduced shrinkage.[57] The opposing trends observed for the OD shrinkage and ID shrinkage substantiate the presence of an asymmetric membrane and imply a gradient in terms of particle packing along the radial direction.

3.4.2.2. Effect of Holding Time

The effect of sintering holding time on dimensional shrinkage was examined. The results of this experiment are presented in Figure 3.11

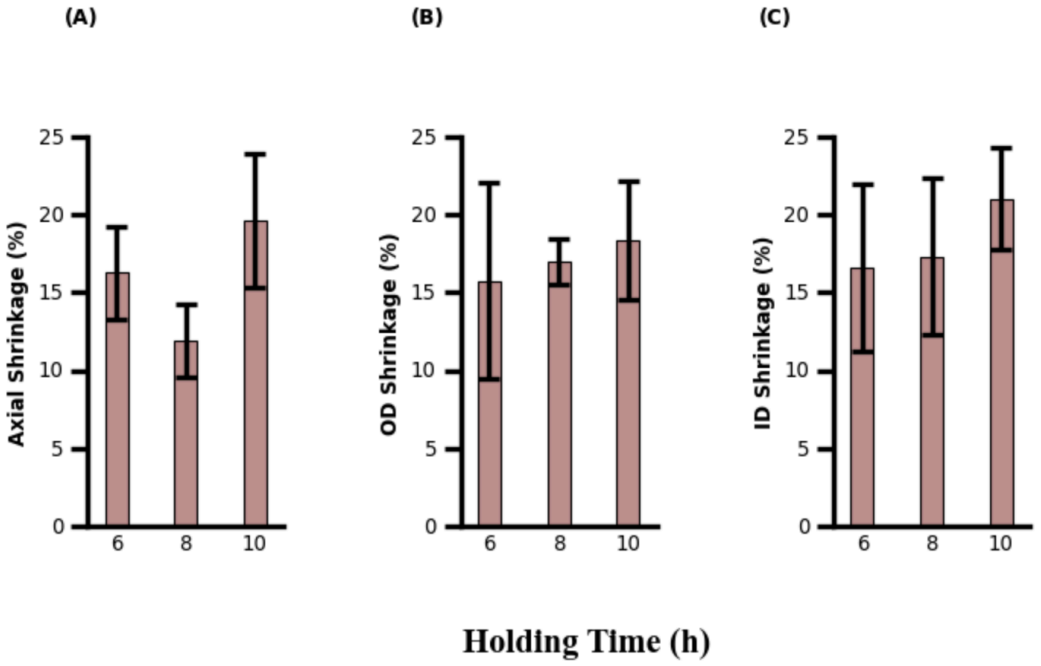

Figure 3.11. The effect of sintering holding time on dimensional shrinkage in the (A) axial direction, (B)radial direction for the outer diameter, and (C) radial direction for the inner diameter. Values provided are an average at a given holding time.

With the exception of the axial shrinkage percentage at a holding time of 8 hours, all samples experienced an average dimensional shrinkage greater than 15% regardless of holding time. Also, with the exception of the axial shrinkage, (due to the 8-hour holding

time) dimensional shrinkage tended to increase with an increase in holding time. This occurrence is in accordance with literature that asserts shrinkage with increased holding time stems from a decrease in the number of pores and an increase in grain growth. [58] Given the outstanding literature and sample variability, the decrease in axial shrinkage at 8 hours of holding time was likely an aberration.

3.4.2.3. Effect of Sintering Temperature

Quantifying the effect of sintering temperature on shrinkage is paramount because minor variations in sintering temperature can result in substantial changes in shrinkage. The effects of sintering temperature on shrinkage in this study are given in Figure 3.12.

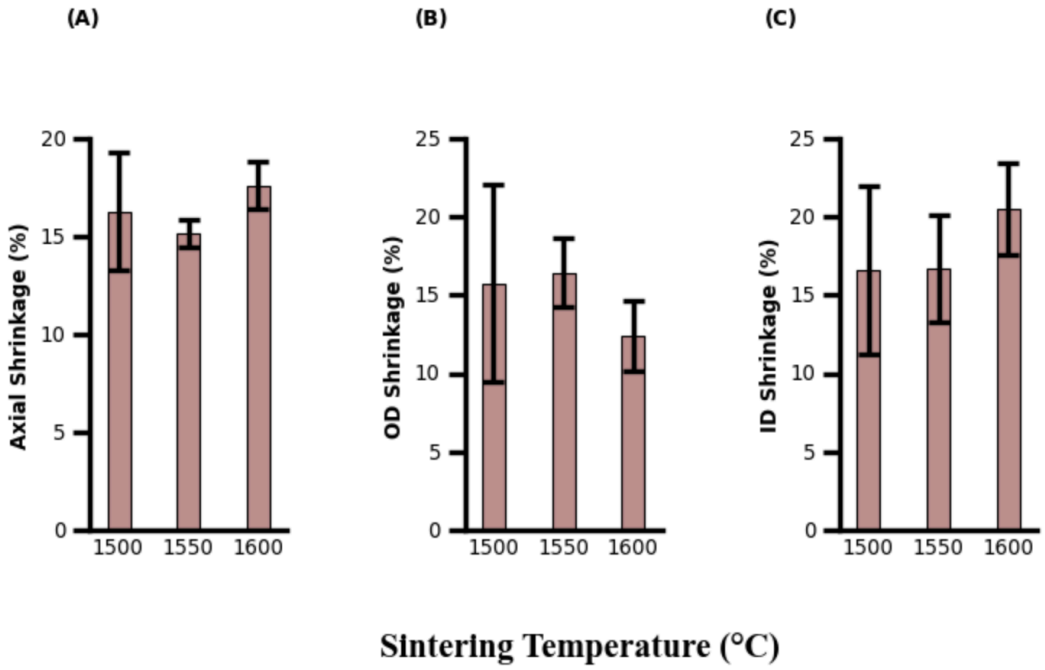

Figure 3.12. The effect of sintering temperature on dimensional shrinkage in the (A) axial direction, (B)radial direction for the outer diameter, and (C) radial direction for the inner diameter. Values provided are an average at a given sintering temperature.

For the axial and inner diameter, maximum shrinkage was observed at a maximum temperature of 1600 °C with axial and inner diameter shrinkages of 17.6 and 20.5%, respectively. This observation is consistent with literature, as an increase in temperature stimulates shrinkage, particle migration, and rearrangement.[59] Despite this observation at 1600 °C, the relationship between temperature and shrinkage was ambiguous. For instance, a minimum outer diameter shrinkage of 16.4% at 1550 °C was not expected. Although the anisotropy of the support may partially explain this, it is more appropriately ascribed to the array of concurrent processes that occur in the latter stages of sintering, some of which are simultaneously a boon and hindrance to shrinkage.[56,60]

3.4.3. Compressive Strength

Compressive strength is the resistance of a material to failure when subjected to compressive forces. Compressive tests are often used for brittle ceramic materials as they are less susceptible to surface defects inherent in ceramic materials.[61,62] Compressive tests are important because they serve as a good indicator of mechanical strength. This study was concerned with determining the ultimate compressive strength of the samples, which is the stress required to rupture.

A Tinus Olsen H25KT Universal Test machine was used to obtain the ultimate compressive strength. Samples were oriented vertically and in contact with the top and bottom platens. In the companion program, specimen dimensions were entered, and the top platen was set to move at a speed of 1 mm/min. Figure 3.13 provides a picture of the setup.

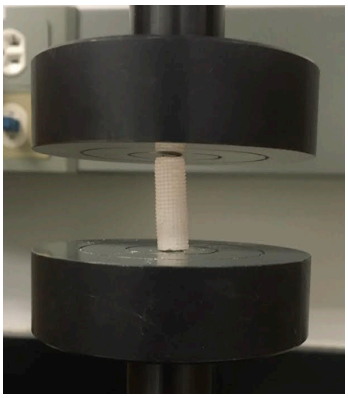

Figure 3.13. Image of compression test setup to determine ultimate compressive strength. The top platen travels at a speed of 1 mm/min.

The companion program provided an output with the changes in position and force during the trial. With the force data, the ultimate compressive strength was calculated with eq (3.2).

$$\sigma_{compressive} = \frac{F_{max}}{A} \tag{3.2}$$

In equation (3.2) ,$\sigma_{compressive}$ refers to the ultimate compressive strength, and F_{max} refers to the maximum force imposed on the sample during the trial. *A* is given by the following:

$$A = \frac{\pi}{4} * (OD^2 - ID^2) \tag{3.3}$$

Equation (3.3) is the radial area of the tube. OD and ID refer to the outer and inner diameter, respectively, of the alumina membrane.

Compression tests were performed on a subset of samples that were fabricated with 25.4 mm long molds. These samples were selected to avoid premature failure due to buckling with high aspect ratio parts.[63] The relationships between compressive strength and solid loading, sintering temperature, and holding time were explored.

3.4.3.1. Effect of Solid Loading

The effect of varying the alumina weight fraction on the ultimate compressive strength was explored. The results are presented in Table 3.4.

Table 3.4. The effect of varying solid loading on the ultimate compressive strength of alumina membranes. Compressive strength values are an average for a given weight fraction.

Weight Fraction (kg/kg)	Compressive Strength (MPa)
0.50	8.10
0.55	10.4
0.60	13.5

Although all the values observed in this study were lower than the compressive strength values of other studies, the trend was consistent with typical observations in literature for ceramic materials.[62,64,65]An increase in solid loading typically leads to more mechanically robust materials.[64,65] In this study, the maximum compressive strength at a weight fraction of 0.60 is likely attributed to improved casting, which resulted in a more homogenous and less porous structure.

3.4.3.2. Effect of Sintering Temperature

Sintering temperature was varied, and the effect on compressive strength was investigated. The results are provided in Table 3.5.

Table 3.5. The effect of varying sintering temperature on the ultimate compressive strength alumina membranes. Compressive strength values are an average for a given sintering temperature.

Sintering Temperature (°C)	Compressive Strength (MPa)
1500	53.2
1550	23.0
1600	17.9

The compressive strength decreased with increasing sintering temperature. This trend is inconsistent with trends in literature as compressive strength and mechanical

properties, in general, increase with sintering temperature. [66–69]Increasing the temperature results in increased densification and reduced porosity, which enhance the sample's mechanical properties.[69] Specimen UID 6, sintered at 1500, likely confounded the results of this particular experiment. From a qualitative standpoint, specimen 6 was perhaps the best-fabricated membrane. It had uniform inner and outer diameters and no apparent cracks or holes. This uniform macrostructure manifested into a study-high compressive strength of 91.46 MPa. This value explains why 1500 °C yielded the highest average compressive strength and the large gap between the other two values. Although significant membrane dissimilarity is not believed to be a pervasive flaw in the compression analysis of this study, this is a drawback of compression analysis with anisotropic samples that are not adequately oriented to achieve 2D isotropy.[63]

3.4.3.3. Effect of Holding Time

Sintering holding time was varied, and the effect on compressive strength was examined. The results are presented in Table 3.6.

Table 3.6. The effect of varying sintering holding time on the ultimate compressive strength alumina membranes. Compressive strength values are an average for a given sintering holding time.

Holding Time(h)	Compressive Strength (MPa)
6	53.2
8	13.5
10	18.3

Contrary to expectations, the holding time of 6 hours had the highest compressive strength at 53.2 MPa. Holding time should increase mechanical strength by decreasing interlayer spacing, the number of pores, and increasing particle size. [58]The population of samples sintered for 6 hours includes sample UID 6. Thus, the issues communicated in 3.4.3.2 apply to this analysis.

3.4.4. Density

Determining the density of the alumina substrates was important because high density typically correlates positively with good mechanical properties.[70] Furthermore, precisely controlling density may improve membrane efficiency for water separations as much as 30 to 40%.[71] Thus, knowing the membranes' density was critical when gauging their potential in subsequent applications.

The density of the membranes was calculated using Archimedes' principle. Archimedes principle states that the buoyant force acting on an object immersed in a fluid is equal to the weight of the displaced fluid.[72] The first step in calculating the density was to take the mass of the dry alumina membrane. Then, the alumina sample was suspended in a beaker of DI water, and the mass was retaken. Once the sample mass in the dry and suspended states was determined, eq. (3.4) was used to calculate the density.

$$\rho_{substrate} = \frac{m_{dry}}{m_{dry} - m_{suspended}} (\rho_{water} - \rho_{air}) \quad \textbf{(3.4)}$$

In eq. (3.4), m_{dry} refers to the dry sample mass in air, $m_{suspended}$ refers to the mass of the sample when suspended in water, ρ_{water} is the density of water, ρ_{air} is the density of air, $\rho_{substrate}$ is the density of the membrane.

Density measurements were obtained for every sample. Descriptive statistical information about the population, irrespective of fabrication parameters, is provided in Table 3.7

Table 3.7. Descriptive statistical information regarding density for the entire population of samples

Min (g/cm^3)	Median (g/cm^3)	Max (g/cm^3)	Mean (g/cm^3)	STD (g/cm^3)
2.42	2.90	3.37	2.89	0.21

Density ranged from 2.42 to 3.37 g/cm^3 with an average of 2.89 g/cm^3. These correspond to moderately strong density values. The effects of solid loading, sintering temperature and holding time on density were also explored.

3.4.4.1. Effect of Solid Loading

The effect of alumina solid loading on the density was explored. It was important to explore this relationship as literature suggests that an increase in solid loading results in an increase in density.[64,65,73]The relationship between these two variables is published in Figure 3.14

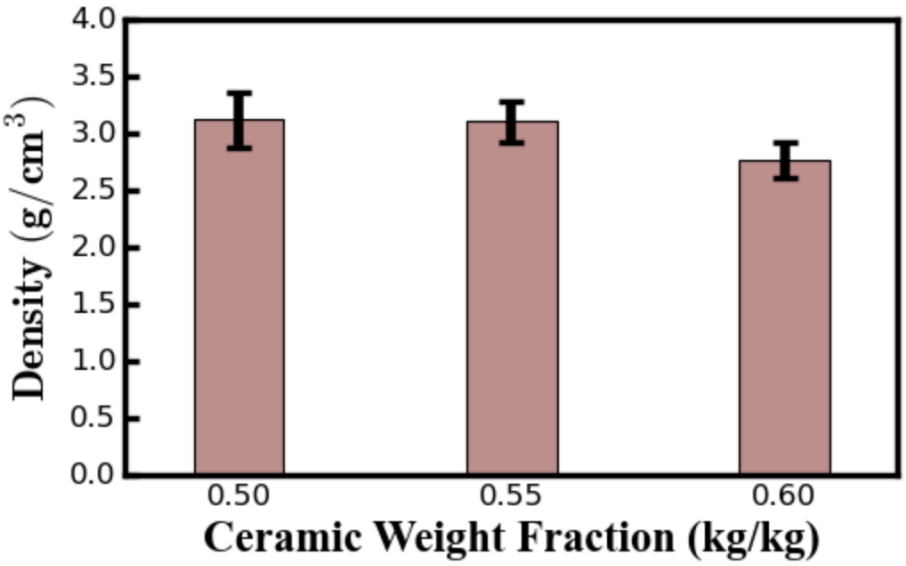

Figure 3.14 Density as a function of alumina solid loading in casting slurry. Values are averages for given weight fraction

Given that a weight fraction of 0.50 had an average density of 3.12 g/cm^3 and a weight fraction of 0.60 had an average density of 2.90 g/cm^3, the findings in this study

did not typify the observations seen in extant literature. In fact, they suggested the contrary as density decreased with an increase in solid loading. However, these results are not necessarily in direct contradiction with prevailing thought as most studies do not communicate the balance of components after increasing the solid loading. In this study, since the ceramic to binder ratio was fixed at 8, an increase in solid loading corresponded to an increase in PVB. Alumina is particularly sensitive to changes in PVB content as a slight rise in PVB weight percentage can significantly increase carbon residue content on the alumina surface during burnout.[31] Residual carbon content is problematic during the sintering phase, where it works to slow the densification rate.[74] Thus, the observed decrease of density with solid loading resulted from increased particle packing not overcoming a pronounced carbon contamination effect. Such findings provide an opportunity to future works to quantify the strength of this effect during the sintering step.

3.4.4.2. Effect of Holding Time

It was essential to investigate the relationship between holding time and density. Holding time provides an alternative means of maximizing density. Increased holding time may be employed in lab setups where necessary sintering temperatures are high and prohibitive. However, the impact of holding time on density on is generally weaker than temperature.[75] Figure 3.15 presents the interaction between holding time and density in this study.

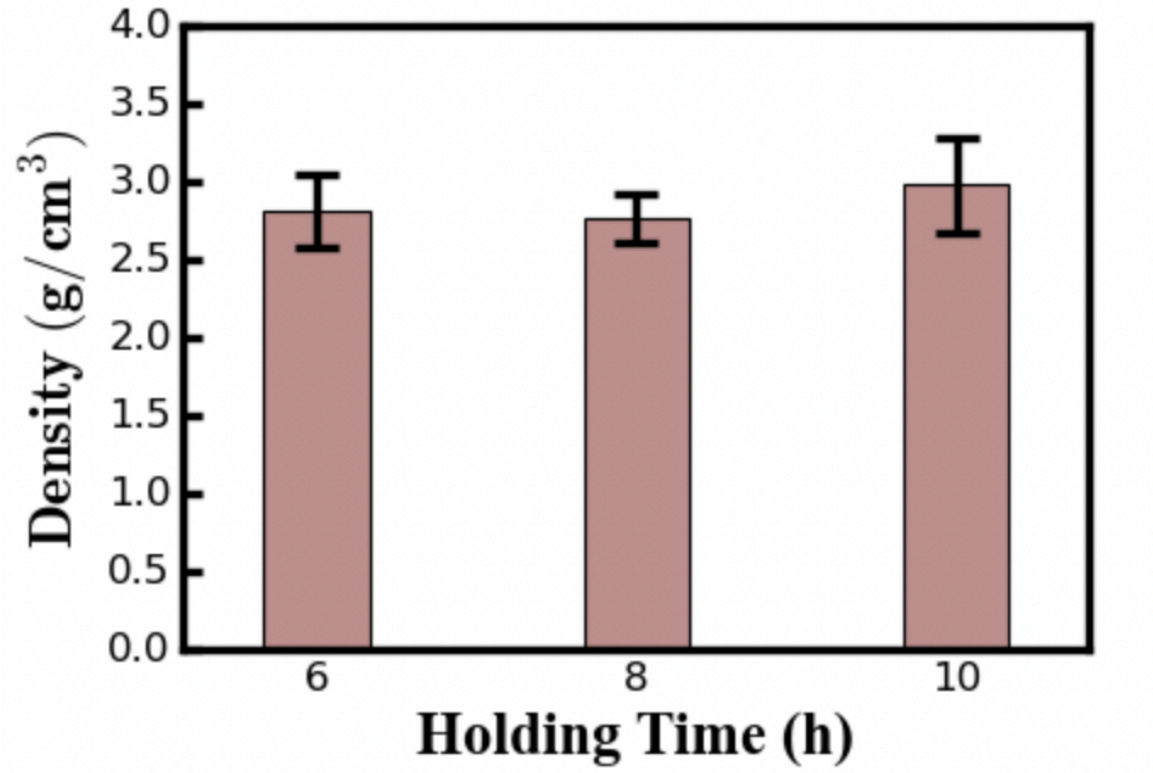

Figure 3.15. Density vs. changes in holding time. Values are averages for given holding time.

In this study, the maximum density observed of 2.97 g/cm^3 occurred at the maximum holding time of 10 hours. This observation is consistent with literature as the maximum time typically allows for more particle rearrangement and hole closure, which lend to a denser membrane.[59,76] Also consistent with the literature is that the effect of holding time is not overwhelmingly strong as the value of 2.97 g/cm^3 is slightly higher than 2.81 g/cm^3 and 2.76 g/cm^3 at 6 and 8 hours, respectively.[75] Despite these observations, the lack of a monotonic increase coupled with sample variability temper the generalizability of these results. A future study could improve upon the reliability of these conclusions by gathering additional data points at each holding time to help distinguish whether the densities are roughly the same or whether a marginal increase in density is indeed observed.

3.4.4.3. Effect of Sintering Temperature

The effect of sintering temperature on density is a commonly explored relationship. An increase in temperature is typically employed to obtain a membrane with maximum density.[20,66–69,75] Thus, it was intriguing and of consequence to determine how this particular system would respond. The results for this relationship in this study are provided in Figure 3.16

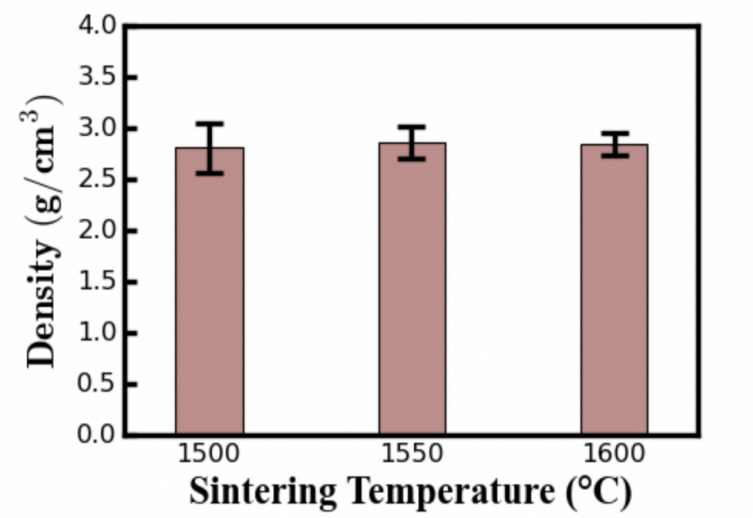

Figure 3.16. Density vs. changes in sintering temperature. Values are averages for given sintering temperature.

Density remained reasonably constant as the sintering temperature increased. The density values ranged from 2.81 g/cm^3 to 2.86 g/cm^3 for the three temperatures. This occurrence was contrary to expectations as the variables, such as viscosity and diffusivity, that promote densification are typically expressed as exponential functions of temperature.[75]However, the results may be reconciled with literature if sintering is viewed as a process with stages. The majority of densification has likely occurred or is occurring at 1500° C. Thus, incrementing the temperature within this range minimally

increases the density.[77] This range likely corresponds to the latter stages of sintering and is predominated by other phenomena, such as grain growth.[77]

3.4.5. Porosity

In this study, porosity refers to "open porosity," which is defined as the fraction of interconnected pore volume to the total bulk volume of the porous material.[78] Porosity is a critical parameter for applications in which fluid must access the pores for successful operation, such as a membrane support.[79] Porosity is also an indicator of mechanical strength, as the two tend to correlate inversely.[80]

The porosity of the alumina samples was calculated via the saturation method. Samples were placed in DI water for 7 hours to ensure pores were fully saturated. The samples were removed from water, and the samples were weighed. Equation (3.5) was used to calculate the porosity.

$$\phi = \frac{m_{saturated} - m_{dry}}{m_{saturated} - m_{suspended}} * 100 \quad \textbf{(3.5)}$$

In eq. (3.5), $m_{saturated}$ refers to the mass taken after the samples were removed from DI water, and ϕ is the porosity. The values for m_{dry} and $m_{suspended}$ were used from earlier density calculations in section 3.4.4.

Porosity measurements were obtained for every sample. Descriptive statistical information about the population, irrespective of fabrication parameters, is provided in Table 3.8

Table 3.8. Descriptive statistical information regarding porosity for the entire population of samples

Min (%)	Median (%)	Max (%)	Mean (%)	STD (%)
18.7	37.9	52.9	35.5	8.59

The porosity in this study ranged from 18.7% to 52.9% with an average porosity of 35.5%. These porosity values are in accordance with other studies that have fabricated tubular alumina membranes through a phase-inversion process.[47] High porosity makes the alumina membranes excellent candidates for substrates in composite membranes. The effects of solid loading, sintering holding time, and sintering temperature on porosity were also explored.

3.4.5.1. Effect of Solid Loading

The effect of solid loading on the porosity of the samples was explored. It was important to explore this relationship because many applications require a balance between maximizing solid loading and maintaining high porosity. The interaction between these variables observed in this study are presented in Figure 3.17.

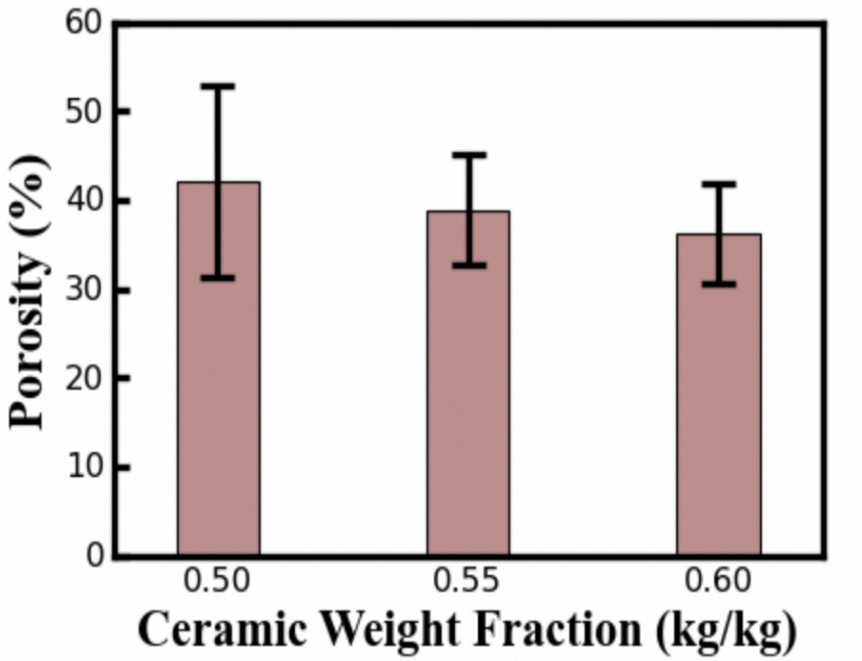

Figure 3.17. Porosity as a function of alumina solid loading in casting slurry. Values are averages for given weight fraction.

Figure 3.17 shows that an increase in solid loading results in a decrease in porosity with a weight fraction of 0.60 having the lowest porosity at 36.2%. The relationship between porosity and alumina solid loading mirrors that of compression strength and alumina solid loading. As discussed, compressive strength and porosity are generally inversely correlated, and this study provides additional credence to this perceived relationship. The increase in alumina particles results in a decrease in alumina particle-particle distance.[73] During sintering, the increased packing of alumina particles allows gaps to be closed more efficiently, thereby reducing porosity.

3.4.5.2. Effect of Holding Time

The response of porosity values to changes in holding time were investigated. Observing the porosity as a function of holding time is important because it provides another piece of information to render a decision regarding final methodology.

Additionally, the relationship between the variables can be difficult to predict as some authors suggest a roughly linear decrease in porosity with increased holding times, while others intimate a parabolic minimum. [58,59,75]The relationship between these variables for this study is shown in Figure 3.18

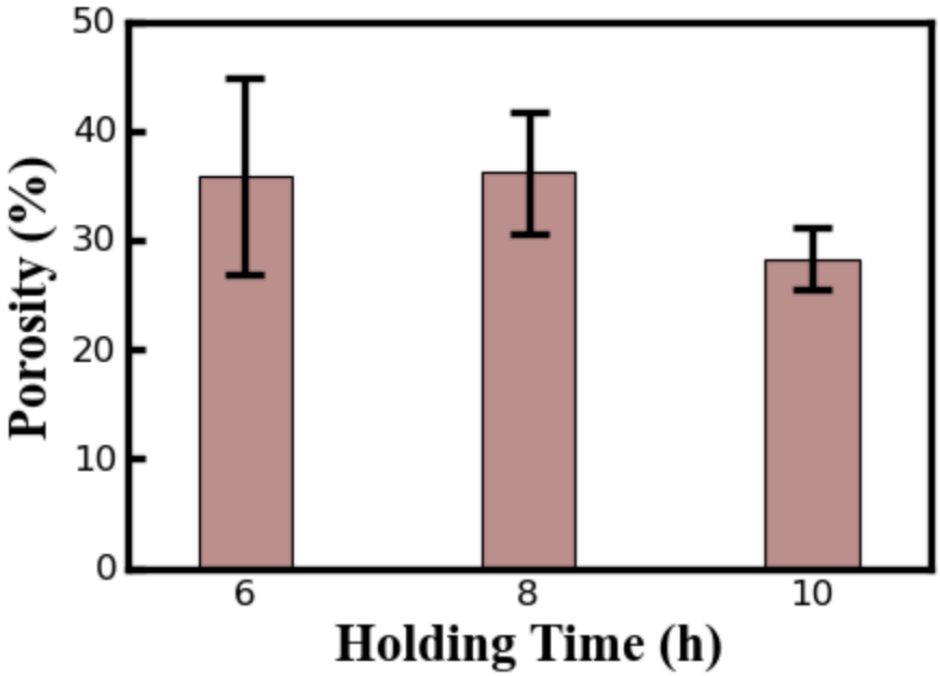

Figure 3.18. Porosity values vs. changes in holding time. Values are averages for given holding time at a fixed sintering temperature of 1500.

As the holding time increased from 6 hours to 8 hours, no substantial change was observed as the averages were similar with similar sample variability. A noticeable change in porosity, however, was detected as the holding time increased from 8 to 10 hours, with porosity reaching a low of 28.3%. These results indicate that appropriate holding times were employed for these alumina green bodies because a parabolic minimum was not observed. This finding implies no deterioration of the underlying microstructure due to abnormal grain growth.[77] [76,81]The low observed at 10 hours may be attributed to the particles having extended time to undergo diffusion.[59,76,81] Thus,

continued analysis of these alumina membranes could explore the extent to which an increase in holding time may be exploited until it leads to deterioration.

3.4.5.3. Effect of Sintering Temperature

The effect of sintering temperature on the membrane porosity was examined. As communicated in section 3.4.4.3 literature suggests that manipulating sintering temperature has a greater impact on properties such as density and porosity. Therefore, it is critical to identify what temperatures are congruent with objectives. Results of this study are presented in Figure 3.19

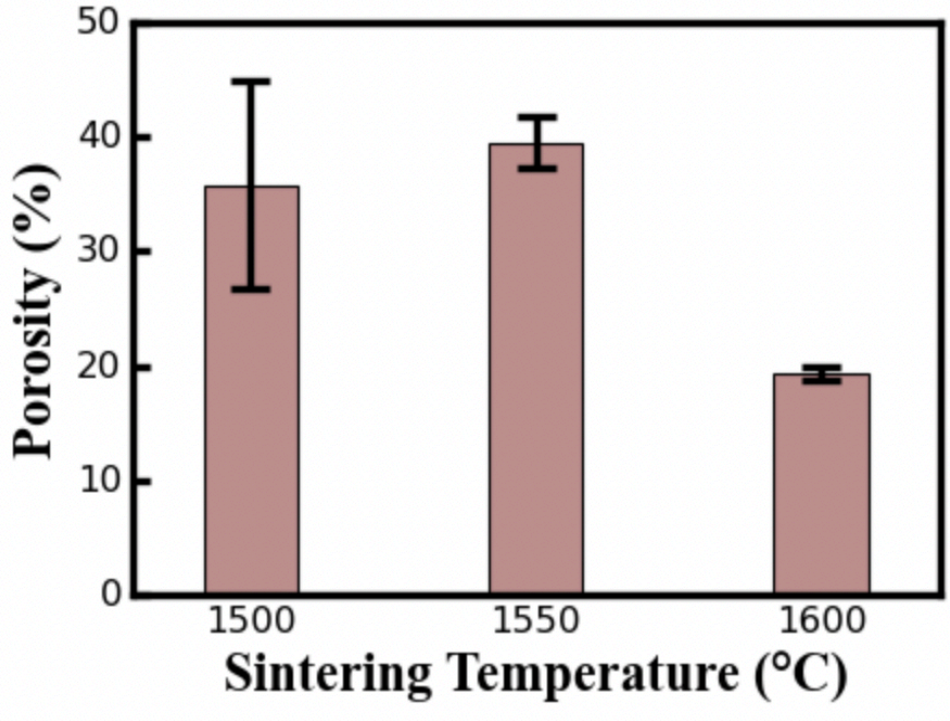

Figure 3.19. Porosity values vs. changes in sintering temperature. Values are averages for given sintering temperature at a fixed holding time of 6 hours

As the sintering temperature increased from 1500 ° C to 1550° C, a slight increase in porosity was observed. From a microstructural perspective, it is unclear what may have led to this slight increase. Ceramic studies that have shown similar behavior have

attributed it to volume expansion. However, this conclusion is incongruent with this study because of the stable density values observed with changing temperature in 4.8.3. Therefore, the notion of volume expansion is rejected, and the observation is deemed a symptom of the inherent variability of the 1500 °C. sample. Discussion from 1500 °C to 1550 °C notwithstanding, the porosity value at 1600 °C of 19.4% did appear to be significant. A porosity value of 19.4% marked a precipitous decline from the porosity values of 35.0+% at the other two temperatures and cannot be rejected due to variability. Furthermore, it gives credence to the theory that sintering temperature has a nonlinear relationship with membrane properties.[75] In future studies, when examining porosity, the methodology employed in this study could be improved by expanding the temperature range and incrementing by 100 °C to clarify the relationship better.

3.4.6. Microstructure

This section will validate earlier observations by supplementing them with Scanning Electron Microscopy(SEM) analysis .SEM is a powerful tool that provides high resolution images of materials at a micrometer scale. The inner surface, outer surface, radial cross section, and pore size distribution were examined with a Tescan XEIA Plasma FIB/SEM machine.

3.4.6.1. Sintering Temperature

The effect of sintering temperature on the inner surface of the alumina supports was examined. As communicated in section 3.4.4.3, the lack of a monotonically increasing trend for density with a rise in temperature may be attributed to grain growth. Thus, it was essential to scrutinize the underlying microstructure to corroborate these claims. The results of this investigation are presented in Figure 3.20.

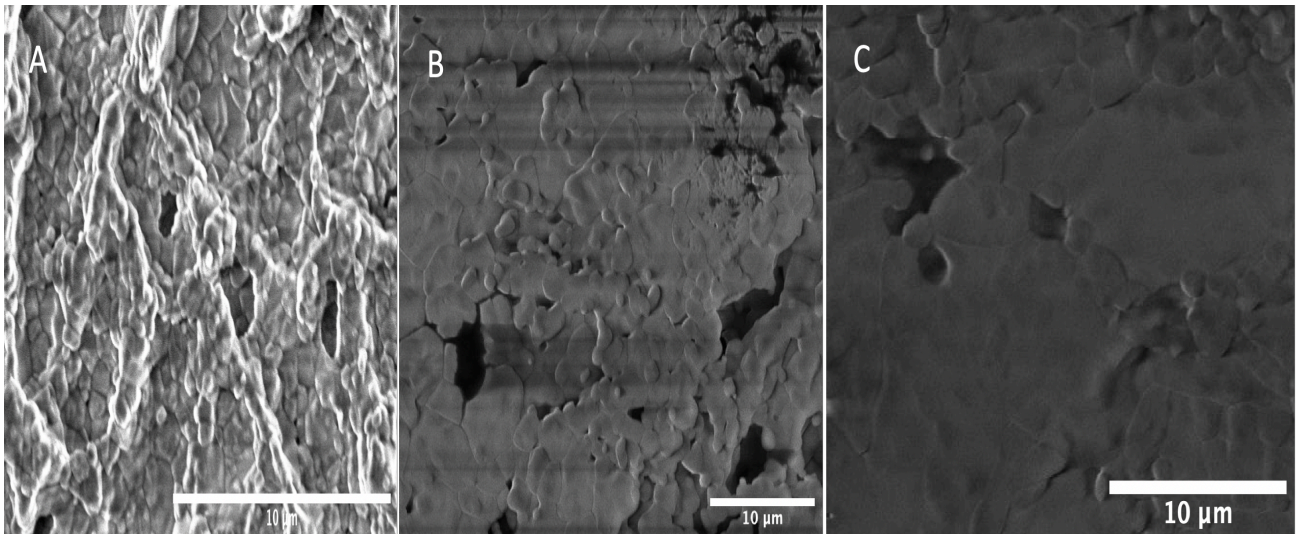

Figure 3.20 SEM images of the inner surface with changes in temperature from (A) 1500 °C, (B) 1550 °C, and (C) 1600 °C Images were obtained 5.0k magnification.

All temperatures exhibited a highly densified inner surface microstructure. There was a slight variation in the densification of the inner surface with an increase in temperature. However, there was a pronounced change in grain size as the temperature increased. As shown in Figure 3.21(A), the grain size at 1500 °C is relatively small, with pores located between grain boundaries. Increasing the temperature to 1550 °C increases grain growth and leads to irregular grain shapes. At 1600 °C, the trend continues as grains are significantly larger and pores become embedded within the grains. Pore occlusion also explains some of the earlier shrinkage observations.

3.4.6.2. Effect of Solid Loading

The change in microstructure of the outer surface with increased solid loading was analyzed. SEM images for this relationship are provided in Figure 3.21

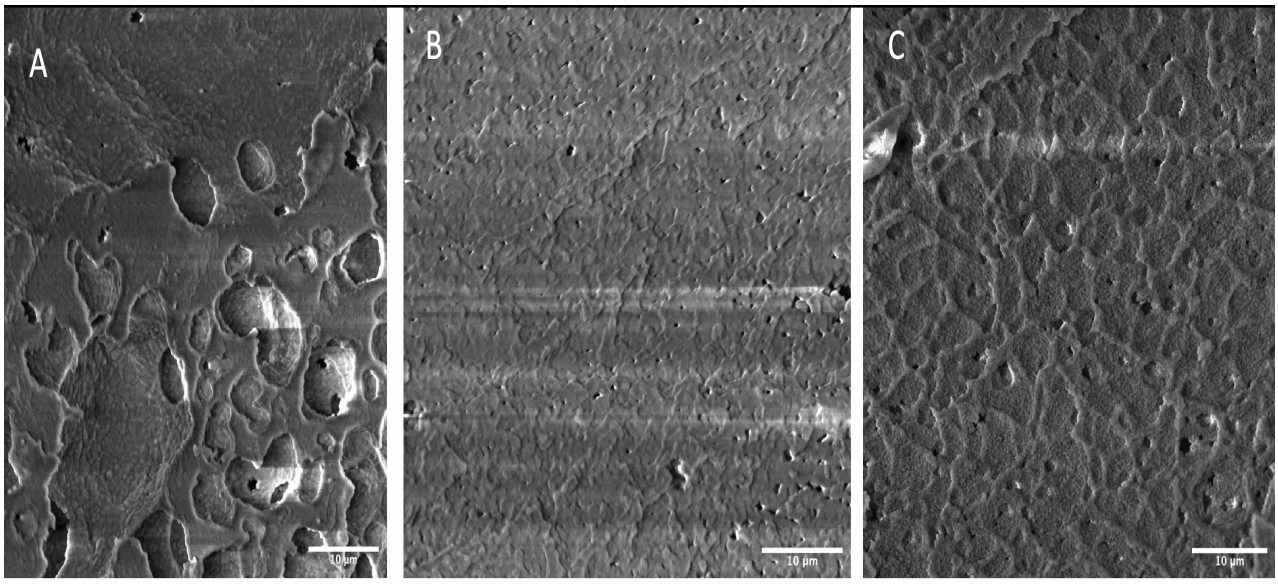

Figure 3.21 SEM images of outer surfaces at (A)0.50 solid loading, (B) 0.55 solid loading, (C) 0.60 solid loading. Images were obtained at 5.0k magnification.

Figure 3.21 shows an improvement in the outer surface microstructure as the solid loading was increased. In Figure 3.21 (A), the outer surface was ravaged by defects, including pinholes, cracks, and craters. At a solid loading of 0.55, in Figure 3.21(B), cracks and craters are not as prevalent. However, pinholes continue to persist and interrupt the continuous structure. These pinholes are also present at a solid loading of 0.60 but to a much lesser extent. Pinholes are problematic because they interrupt the continuous microstructure, which can lead to weakened mechanical strength and coating difficulty.

The SEM images were also used to determine the pore size distribution for the outer surface at various solid loadings. To determine the pore sizes, images at 10.0k magnification were scaled using Image J. The threshold on these images was then adjusted to establish a binary color gradient, where the outlines of the pores are colored red. Once the pores were isolated from the background, the diameter was measured using the built-in Image J analysis tools. The results of this procedure are provided in Table 3.9.

Table 3.9 Descriptive statistical information regarding pore size distribution for different solid loadings

Solid loading	Min (μm)	Median (μm)	Max (μm)	Mean (μm)	STD (μm)
0.50	3.50	8.54	38.8	10.3	5.95
0.55	1.21	1.97	6.31	2.46	1.33
0.60	0.50	1.46	6.22	1.75	1.02

As seen in Table 3.9, variability in pore size increases with a decrease in solid loading. Low solid loadings led to a broad pore size distribution. A broad pore size distribution portends poorly for separation performance because it increases the permeability of the membrane.[82]

3.4.6.3. Cross Section

The cross-sections of the tubular supports were investigated to determine if the anisotropic microstructure was visible in the radial direction. Examination of the cross-section would allow for comparison with other studies as the radial cross-section is typically used to determine the presence of finger-like or sponge-like pores. Different magnifications of the radial cross-section are presented in Figure 3.22

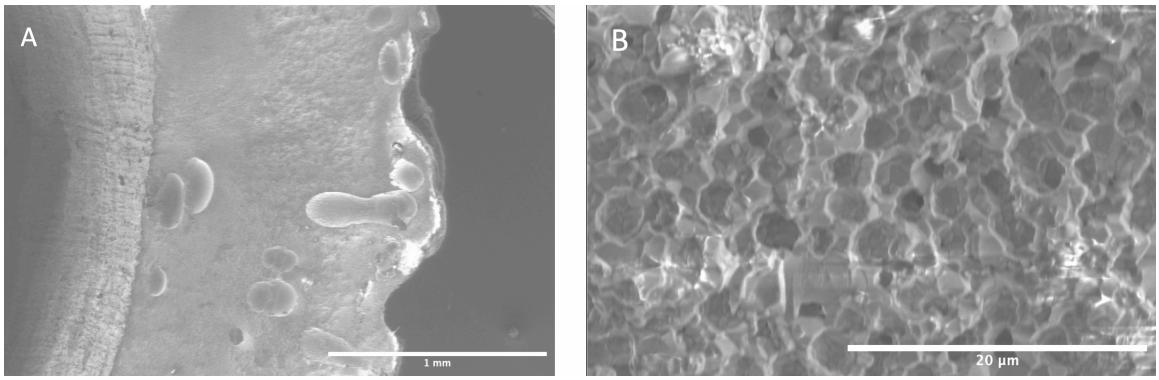

Figure 3.22. Radial cross-section at magnifications of (A) 50x and (B) 2500x.

Figure 3.22 (A) However, there are very few of these voids, and they do not traverse the circumference of the outer cylinder. Figure 3.22 (B) provides a close-up of this region but no additional evidence other than well-defined grains of roughly the same shape. Thus, it was concluded that neither finger-like nor sponge-like pores were observed from the radial SEM images. This occurrence was unexpected, but it was not without precedent as Zhu et al. also did not observe pores with a definite shape. They attributed these observations to the thickness of the membrane. This explanation may also apply since this study also had membranes of 1 mm to 2 mm in thickness.

3.5. Conclusions

This chapter delineates a reliable and repeatable procedure that could use the 3D printed mesh cylinder from chapter 2 and yield an alumina substrate. A schematic of the process is provided in Figure 3.23.

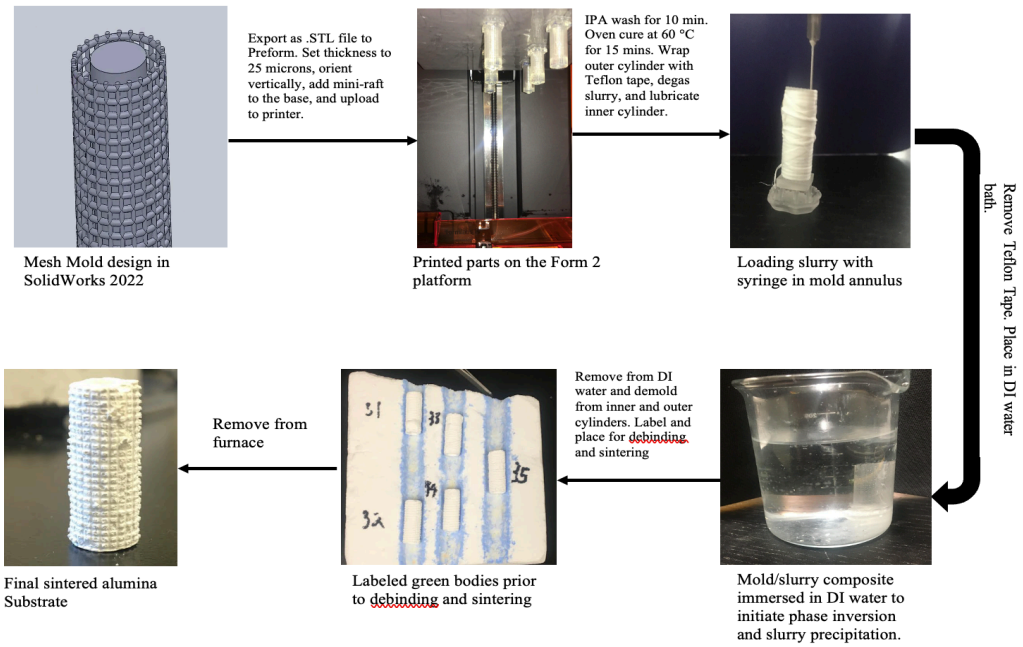

Figure 3.23 Schematic of Fabrication Procedure.

The iterative approach limited the potential sources of variability, which helped to consistently produce alumina substrates. The substrates were characterized extensively and relationships between manipulated variables and sintered properties were illuminated. From this characterization it was clear that 3D printing imposed a tangible surface roughness, allowed for well-defined radial features, and provided high repeatability. Furthermore, the microstructure of the substrates could be tailored with solid loading, holding time, and sintering temperature. The ideal combination of these independent variables was a solid loading of 0.60, holding time of 6 hours and sintering temperature of 1500. This combination of variable values reinforced the substrate with good density, porosity(>30%), and compressive strength, all of which were necessary for practical application.

Chapter 4: LTA Composite Membrane for Ethanol-Water Pervaporation Separation

This chapter will discuss how the fabricated alumina substrates were employed as supports zeolite membrane deposition for an ethanol-water pervaporation separation process.

4.1. Introduction

Liquid-liquid separation and purification are critical to many industrial processes. However, many liquid-liquid separation steps are energy-intensive, thermodynamically limited, and detrimental to the environment.[83,84] Membranes have garnered a significant amount of interest as cheaper, cleaner, and more efficient alternatives.[85]Alumina membranes, in particular, are highly desirable because they are thermally stable, chemically stable at low pH, and do not swell.[84]These characteristics make asymmetric alumina membranes excellent candidates for pervaporation.

Pervaporation is the separation of a liquid mixture by partially vaporizing it through a nonporous selective membrane. A generalized lab-scale schematic is provided in figure 5.1.

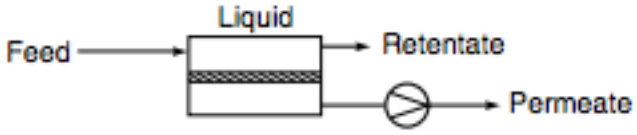

Figure 4.1 Lab-scale schematic of the pervaporation process. Adapted from ref. 7

The driving force behind pervaporation is the difference in partial pressures between the permeate side and feed side. At a lab scale, this pressure difference is maintained by vacuum pumping on the permeate side. The selectivity of the membrane is

governed by the permeability of the components in the feed stream. This makes pervaporation particularly intriguing as it can potentially separate close-boiling point and azeotropic mixtures. As the demand for sustainable energy alternatives increases, ethanol-water separation to yield anhydrous ethanol becomes increasingly important. This separation will be discussed herein.

Although the fabricated alumina membranes could be used in their present condition, their porosity is not ideal for ethanol-water separation and would result in poor separation.[86]It is much more effective to coat the alumina membranes with a thin dense selective layer and use the alumina membranes as a mechanical support.

Zeolites, crystalline aluminosilicate materials, are often used as selective layers owing to their tunable functionalities, stability under harsh conditions, and well-defined pore size. Of the class of zeolites, Zeolite A(LTA) has drawn attention in separations related to polar molecules because of its high hydrophilicity. More specifically, LTA has demonstrated excellent performance in ethanol/water pervaporation, achieving separation factors greater than 10,000.[5] Thus, this chapter will explore the pervaporation performance of LTA selective layers on the alumina membranes.

4.2. Experimental

4.2.1. Materials

Silicic acid hydrate – 100 Mesh Powder (SiO_2 x H_2O), sodium hydroxide (NaOH, flake, 98%), aluminium isopropoxide ($Al[OCH(CH_3)_2]_3$, 98+%), and tetramethylammonium hydroxide (TMAOH, $C_4H_{13}NO$, 25% w/w aq.), were obtained from Alfa Aesar. LUDOX Silica (AM-30) and sodium aluminate were obtained from Sigma Aldrich.

4.2.2. Zeolite Synthesis

Zeolite membrane synthesis began with zeolite seed preparation. Precursors NaOH, TMAOH, SiO_2 x H_2O and H_2O were added to a perfluoxy copolymer (PFA) bottle and allowed to mix for approximately 8 hours on a magnetic stirrer. Once a clear homogenous solution was obtained, aluminum isopropoxide was added to the solution and stirred for 6 hours. After 6 hours, a clear gel with a molar composition of 11.25 SiO_2: 1.8 Al_2 O_3:6.7$(TMA)_2O$:1.2 Na_2O:700 H_2O. The gel was transferred to a convection oven at 70 °C, where it remained for 72 hours. Using repeated centrifugation at 5000 rpm for 15 minutes, the seeding crystals were purified and concomitantly washed in DI water until the pH was below 9. Finally, the seeds were calcined at 550 °C for 6 hours.

To form a colloidal suspension, 1.96% of zeolite seeds by weight were added to a balance of water. The alumina substrates were dipped in the colloidal suspension 5 times to coat both the inner and outer surfaces of the substrate. The coated alumina substrate tubes are then allowed to dry at room temperature for 48 hours.

To develop the zeolite membrane on the alumina substrate, sodium aluminate and NaOH were added to the required amount of water and mixed on a magnetic stirrer for 15 minutes. While still mixing, Ludox silica was slowly added dropwise. After 12 hours of mixing, a clear gel with a molar composition of 5 SiO_2: $1Al_2O_3$:$50Na_2O$:$1000H_2O$ was obtained. The gel and seeded alumina tubes were transferred to an autoclave, where hydrothermal growth occurred at 100 °C for 5 hours. The tubes were subsequently washed several times with DI water and dried over 8 hours at 60 °C.

4.2.3. Pervaporation Tests

Prior to setting up the apparatus for pervaporation, an ethanol-water mixture with a 90:10(ethanol to water) weight composition was prepared. Büchner flasks were weighed so permeate masses could be determined after a predetermined set time of 1 hour.

For the pervaporation setup, the composite alumina membrane was immersed into the ethanol-water mixture in an oven at 70 °C. With stainless steel pipes, the membrane was connected to the necks of 2 Büchner flasks. One Büchner flask was used to capture the transient permeate; while the other was used to capture the steady-state permeate. The Büchner flasks were kept in cold traps that used liquid nitrogen to condense the permeate vapor. The side arms of the Büchner flasks were attached to a vacuum pump to maximize the pressure gradient on the permeate side. A schematic representation of the experimental setup is provided in Figure 4.2.

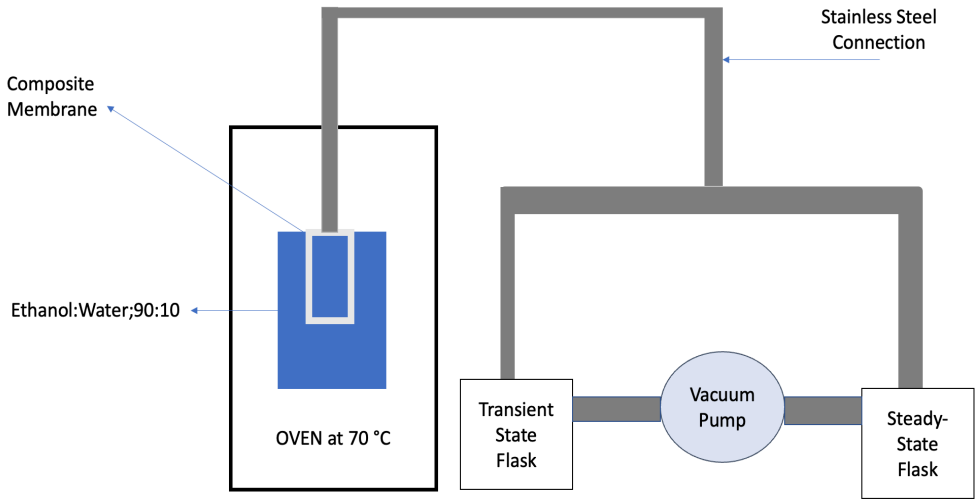

Figure 4.2 Schematic of Pervaporation setup.

Once the experiment was initiated, 10 minutes were allotted for the system to reach steady state. At this point, flow was redirected from the Büchner flask

corresponding to the transient state to the Büchner flask corresponding to the steady state. The system remained in this state for 1 hour at which point the experiment was complete and samples were analyzed.

4.2.4. Pervaporation Analysis

Immediately after the pervaporation experiment ended, the steady state Büchner flask was weighed to capture the mass of the effluent permeate stream. With this additional information, the total mass flux was calculated:

$$J'' = \frac{m_p}{A * t} \tag{5.1}$$

In equation 5.1, m_p corresponds to the mass of the permeate, A is the membrane surface area, and t is the allotted time. Afterwards, the concentrations in the effluent permeate stream were determined with gas chromatography (Agilent Technologies 7890A). For each sample, 2 injections were taken and averaged. The area under the peaks of the chromatograph output was calculated and then compared to a calibration curve to determine the concentration. With the concentrations, separation performance was calculated with the following:

$$\alpha = \frac{y_a/y_b}{x_a/x_b} \tag{5.2}$$

Equation 5.2 is the ratio of the mass fractions in the permeate phase to the ratio of the mass fractions in the feed stream. In equation 5.2, y and x refer to permeate and feed compositions, respectively.

4.3. Results and Discussion

4.3.1. Independent Performance of Alumina Substrate

The performance of the alumina substrate without zeolite coating was assessed to test the hypothesis that the substrate would perform poorly without a selective layer. Determining the alumina support's independent performance was vital because it would clarify the zeolite layer's efficacy and prevent alumina's inherent hydrophilic character from confounding results. Table 4.1 presents the flux and separation factor for the independent run.

Table 4.1 Separation performance for alumina support 37 prior to zeolite coating

UID	Flux (kg/(m^2•h))	Separation Factor(kg/kg)
37	26.2	1.10

Although high flux and low separation were expected, the results in Table 4.1 neared extremes. Even in systems where the support is also used as the separation layer, it is not uncommon to see low fluxes in the range of 1 kg/(m2-•h)) to 10 kg/(m2-•h)).[87] Thus, the large flux and decreased permeation resistance suggested the presence of macrovoids, perhaps to an extraordinary extent. In any case, these results were promising as they confirmed that the effect of the zeolite layer would be isolated and portended good substrate function.

4.3.2. Performance of The Ceramic Membrane

The pervaporation performance of the composite membrane after one zeolite growth cycle was gauged. Information from this experiment would indicate whether the

3D fabricated alumina support could be used in practical applications, especially with a separation layer that is particularly sensitive to the properties of the support. The flux and separation factor for this experiment are provided in Table 4.2

Table 4.2 Separation performance for alumina support 37 after one cycle of zeolite coating.

UID	Flux (kg/(m^2•h))	Separation Factor(kg/kg)
37	0.800	5190

With a value of 0.800 kg/((m2•h)), the flux was markedly lower than that without zeolite coating. This finding suggested that a dense zeolite layer had, in fact, grown on the alumina support. Further evidence of successful zeolite deposition is provided by the separation factor of 5190. Not only do the results suggest the alumina support with a coated zeolite layer can facilitate the separation of water from ethanol, but they are also consistent with the oft-observed tradeoff between flux and separation in literature. To further contextualize the results, they were compared against other alumina/separation layer pairings for ethanol dehydration in Table 4.3.

Table 4.3 Performance data for the dehydration of ethanol on α-Alumina supports from various studies

Membrane Support	Separation Layer	Flux(kg/(m^2•h))	Separation Factor(kg/kg)	Temperature (°C)	Reference
α-Alumina	Zeolite A	2.15	10,000	75	88
α-Alumina	Zeolite X	0.89	360	75	88
α-Alumina	Zeolite Y	1.59	130	75	88
α-Alumina	PVA	1.05	38	70	89
α-Alumina	NaA	3.80	3600	125	90
α-Alumina	Zeolite A	0.80	5190	70	This Study

Table 4.3 indicates that despite the defects communicated in chapter 4, the alumina support in this study functioned well enough to exploit the selective permeability of zeolite A separation layers. This study's separation factor of 5190 outperformed other hydrophilic separation layers on a-Alumina, such as zeolite X, zeolite Y, NaA, and PVA. However, Table 4.3 also indicates that zeolite A's separation ability is not maximized in this study, as Tanaka and colleagues achieved a separation factor of 10,000 with an increased flux of 2.15 kg/(m2-•h)).[88] This suggests that the support morphology can be improved to foster better zeolite growth, leading to better performance.

4.3.3. Microscopic Analysis of Zeolite Deposition

To confirm the deposition of the zeolite layer onto the support, the composite membranes were analyzed via SEM. SEM images of the coated substrate along with a bare support for comparison are provided in Figure 4.3

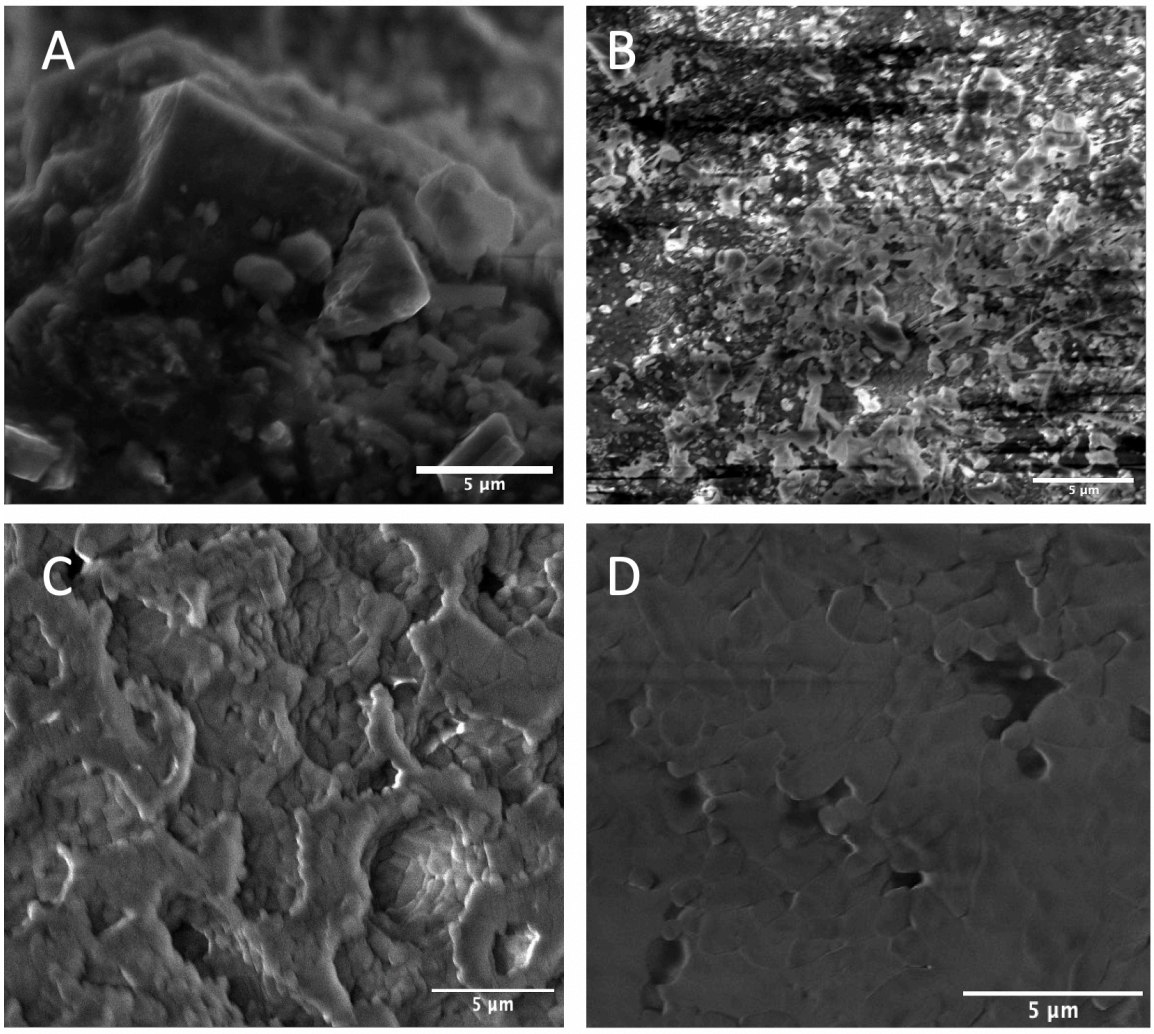

Figure 4.3 SEM images of coated and bare substrates. (A) Outer surface of coated Support UID 37, (B) Inner surface of coated Support UID 37,(C) Outer surface of bare Support UID 38,(D) Inner surface of bare Support UID 38. All images were obtained at 10.0k magnification with the exception of (B) which was obtained at 4.99k magnification.

In Figure 4.3, UID 38 was used for comparison because it was fabricated under identical conditions and should have a similar microstructure. A distinct zeolite layer was observed on the inner and outer surfaces. SEM images in Figure 4.3(A) and (B) reveal the crystalline cubic morphology of LTA.[91] Based on the SEM images, the crystal size is roughly 2.5 µm. The crystal size in agreement with the findings of Yu et. Al. who argue that a TMAOH/NAOH of approximately 50, such as the one used in this study, should

result in a crystal size around 2 μm.[92] Knowledge of the crystal size is important because it controls the diffusivity and adsorption of feed components.[92] Furthermore, smaller crystals lead to more uniform zeolite layers.[92] However, a unform zeolite layer was not observed on the smooth inner surface as expected. As shown in Figure 4.3(B), the zeolite crystals are interspersed on the alumina support. Discontinuity in the zeolite surface is not ideal for separation performance.

4.4. Conclusions

This chapter aimed to identify alumina substrates that could be used in a separation process of practical significance. The substrates were coated with zeolite A and employed in a pervaporation process to separate water from an ethanol feed. The results indicate that the 3D printed alumina substrates with zeolite coating could achieve robust performance for ethanol dehydration that is comparable, if not better, than other α-alumina composite systems.

It was critical to first determine if the substrate was viable in a pervaporation process as the requirements of the support are less stringent.[85] Even with less stringent requirements, expectations were tempered given the factors challenging favorable results, including macropores, dents and defects, and surface roughness.[5] Despite these challenges, the membrane's performance and SEM images indicated that a seed-assisted growth method could lead to successful zeolite deposition on the alumina support, but it did impugn the perceived need for a smooth and uniform surface when dip coating the seed solution. As previously communicated, substrate roughness was perceived to be a challenge to overcome for zeolite deposition. However, this was not observed as the highly ordered roughness imposed by 3D printing led to a complex interaction between

the support and zeolite layer that was conducive to zeolite deposition. [53,54,93,94]This study's methodology was limited in that its analysis of this behavior was merely qualitative. Future studies could build upon these findings by quantifying the impact of alumina-support patterning on LTA deposition.

Chapter 5: Conclusions and Future Work

5.1. Conclusions

This thesis aimed to develop a unique design and procedure for the fabrication of alumina substrates that exploited the accuracy and precision of 3D printing without being prohibitively limited by the constraints of a particular printer. In addition, this study sought to employ the fabricated substrate in a practical separation procedure not only as a proof-of-concept but also to highlight the advantages of 3D printing. Preliminary fabrication tests indicated the mesh cylinder via the alternative approach provided the best chance of consistently producing alumina substrates. Chapter 4 validated this theory as multiple substrates were produced with similar dimensions, roughness, durability, and underlying microstructure. Then, the substrates were coated with LTA and underwent pervaporation performance testing where they demonstrated that they could reasonably separate water from ethanol. The results of this study suggest that the research objectives were realized. The success of this study validates indirect fabrication as a viable lab-scale alternative to fabricating separation membranes with performance comparable to other fabrication techniques.

The study was not without its limitations. As communicated in the introduction, generalizability is limited to applications involving the Form 2. SLA printing is in the upper echelon of printing technologies concerning resolution. Printers with lower resolution may not yield supports with the same degree of repeatability and reproducibility. Moreover, the research conducted in this study was performed to establish feasibility. Thus, there were a number of topics that were broached but not fully explored. The following section will provide future directions for these topics.

5.2. Future Work

To advance this study in the future, the following research directions can be explored.

(1) Reversal of asymmetric structure: The conclusions in chapter 2 may be expounded upon by designing a new mold that would allow for the reversal of the microstructure observed in this study. This may be accomplished by meshing the inner cylinder and rendering the outer cylinder solid. Although the solid outer cylinder was unable to be demolded in this study, future studies could attempt to make the outer cylinder sufficiently thin to make demolding feasible. If this is still unsuccessful, studies could adapt a similar demolding procedure to this study where the outer cylinder is lubricated, the inner mesh cylinder struts are broken, and the support is demolded by pulling on the inner surface. In any case, a successful study of this alternative design would provide further evidence of indirect fabrication's ability to tailor the microstructure of final parts.

(2) Procedural Optimization: There are several options in which future studies could explore the topics of chapter 3. This section will focus on implementing additives and membrane fabrication for other systems.

Although the procedure in this study was manipulated to limit the variability incurred during loading and immersion precipitation steps, future research could build upon this by incorporating additives. No dispersants, sintering additives, or co-binders were used in this study because feasibility with the indispensable components needed to be established. Now that it has been established, an additive such as polyethylene glycol (PEG), which is often used as a co-binder in PVB/Alumina systems, may be incorporated.[95] The introduction of PEG could improve the rheological behavior of the

slurry or reduce the PVB-induced carbon contamination believed to have influenced this study. This would expand the working knowledge of what sintered properties are attainable with this system and the derivatives of this system.

Conceivably, the technique employed in this study is compatible with any ceramic or polymer, provided it is in a flowable system. Thus, researchers could attempt to fabricate membranes of polymer and ceramics that are notoriously difficult to fabricate traditionally. This would corroborate that the technique in this study is versatile and virtually untethered.

(3) Performance Enhancement with Well-Patterned Roughness: As communicated in chapter 4, roughness can lead to a complex interaction that enhances the deposition of colloidal materials[52,53,94]. Thus, researchers could explore how 3D-printing imposed roughness influences the deposition of separation layers. This would differ from previous roughness studies as they did not have comparable control to impose and pattern this roughness. A roughness study may be coupled with an issue in composite membranes, such as the inner surface coating of seed-assisted zeolite.

In some applications, it is beneficial to coat the inner wall with the zeolite layer because it protects the zeolite layer from mechanical damage.[5] However, conventional seeding deposition methods such as dip coating are not as effective when coating the inner surface. Researchers could use a design similar to the one presented in 0 to impose roughness on the inner cylinder and assess its effect on seed deposition. Such a study would be impactful as it would provide an alternative solution with enhanced reproducibility to a commonly encountered problem in zeolite deposition.

References

1. Liang B, He X, Hou J, et al. Membrane Separation in Organic Liquid: Technologies, Achievements, and Opportunities. *Advanced Materials*. 2019;31(45):1806090. doi:10.1002/ADMA.201806090

2. Sholl DS, Lively RP. Seven chemical separations to change the world. *Nature 2016 532:7600*. 2016;532(7600):435-437. doi:10.1038/532435a

3. Kayvani Fard A, McKay G, Buekenhoudt A, et al. materials Inorganic Membranes: Preparation and Application for Water Treatment and Desalination. doi:10.3390/ma11010074

4. Ruys AJ. Introduction to metal-reinforced ceramics. *Metal-Reinforced Ceramics*. Published online January 1, 2021:1-20. doi:10.1016/B978-0-08-102869-8.00001-X

5. Wenten IG, T Dharmawijaya ab P, P Aryanti PT, Mukti bd RR. LTA zeolite membranes: current progress and challenges in pervaporation. 2017;7:29520. doi:10.1039/c7ra03341a

6. Tennison SR. MICROPOROUS CERAMIC MEMBRANES FOR GAS SEPARATION PROCESSES. Published online 1996.

7. Baker RW. MEMBRANE TECHNOLOGY AND APPLICATIONS SECOND EDITION.

8. Femmer T, Kuehne AJC, Wessling M. Lab on a Chip TECHNICAL INNOVATION Print your own membrane: direct rapid prototyping of polydimethylsiloxane. 2014;14:2610. doi:10.1039/c4lc00320a

9. Low ZX, Chua YT, Ray BM, Mattia D, Metcalfe IS, Patterson DA. Perspective on 3D printing of separation membranes and comparison to related unconventional fabrication techniques. *J Memb Sci*. 2017;523:596-613. doi:10.1016/J.MEMSCI.2016.10.006

10. Wee Koo J, Shin Ho J, An J, Zhang Y, Kai Chua C, Haur Chong T. A review on spacers and membranes: Conventional or hybrid additive manufacturing? *Water Res*. 2021;188:116497. doi:10.1016/j.watres.2020.116497

11. Lee JY, See Tan W, An J, et al. The potential to enhance membrane module design with 3D printing technology. Published online 2015. doi:10.1016/j.memsci.2015.11.008

12. Hoek EM v, Pendergast MM. *INTRODUCTION 1 WHAT IS A MEMBRANE?*; 2013.

13. Design specifications for 3D models (Form 2). Accessed November 6, 2022. https://support.formlabs.com/s/article/Design-Specs?language=en_US

14. Wang X, Huang D, Wang L, Meng X, Lv Y, Xia S. Modeling of the fouling of inside-out hollow fiber UF Membranes. *Water Sci Technol Water Supply*. 2017;17(1):300-310. doi:10.2166/ws.2016.137

15. Rezaei B, Pan JY, Gundlach C, Keller SS. Highly structured 3D pyrolytic carbon electrodes derived from additive manufacturing technology. *Mater Des*. 2020;193. doi:10.1016/J.MATDES.2020.108834

16. Form 2: Affordable Desktop SLA 3D Printer. Accessed November 5, 2022. https://formlabs.com/3d-printers/form-2/

17. Krieger KJ, Bertollo N, Dangol M, Sheridan JT, Lowery MM, O'Cearbhaill ED. Simple and customizable method for fabrication of high-aspect ratio microneedle molds using low-cost 3D printing. *Microsyst Nanoeng*. 2019;5(1). doi:10.1038/S41378-019-0088-8

18. 3D Printing Overhang: How to 3D Print Overhangs | All3DP. Accessed November 6, 2022. https://all3dp.com/2/3d-printing-overhang-how-to-master-overhangs-exceeding-45/

19. Chi Y, Li T, Wang B, Wu Z, Li K. Morphology, performance and stability of multi-bore capillary La0.6Sr0.4Co0.2Fe0.8O3-Δ oxygen transport membranes. *J Memb Sci*. 2017;529:224-233. doi:10.1016/J.MEMSCI.2017.02.010

20. Xue LA, Chen IW. Low-Temperature Sintering of Alumina with Liquid-Forming Additives. *J Am Cerom Soc*. Published online 2011:74.

21. Pulgarín HLC, Albano MP. Sintering and Microstrusture of Al2O3 and Al2O3-ZrO2 Ceramics. *Procedia Materials Science*. 2015;8:180-189. doi:10.1016/j.mspro.2015.04.062

22. Li H, Liu Y, Liu Y, Zeng Q, Liang J. Thermal Treatment of γ-Al2O3 for the Preparation of Stereolithography 3D Printing Ceramic Slurries. *Front Mater*. 2019;6. doi:10.3389/fmats.2019.00295

23. Seniutinas G, Weber A, Padeste C, Sakellari I, Farsari M, David C. Beyond 100 nm Resolution in 3D Laser Lithography-Post Processing Solutions.

24. Danninger H, Gierl-Mayer Dr C. Advanced powder metallurgy steel alloys. *Advances in Powder Metallurgy: Properties, Processing and Applications*. Published online January 1, 2013:149-201. doi:10.1533/9780857098900.2.149

25. Tan X, Liu S, Li K. Preparation and characterization of inorganic hollow fiber membranes. *J Memb Sci*. 2001;188:87-95.

26. Liu S, Li K, Hughes R. Preparation of porous aluminium oxide (Al 2 O 3) hollow fibre membranes by a combined phase-inversion and sintering method. doi:10.1016/S0272-8842(03)00030-0

27. Jouyban A, Fakhree MAA, Shayanfar A. *Review of Pharmaceutical Applications of N-Methyl-2-Pyrrolidone*. Vol 13.; 2010. www.cspsCanada.org

28. Mamah SC, Goh PS, Fauzi Ismail A, Yogarathinam T, Raji YO, El-Badawy H. Recent development in modification of polysulfone membrane for water treatment application. *Journal of Water Process Engineering*. 2021;40:101835. doi:10.1016/j.jwpe.2020.101835

29. Febriasari A, Huriya, Ananto AH, Suhartini M, Kartohardjono S. Polysulfone–Polyvinyl Pyrrolidone Blend Polymer Composite Membranes for Batik Industrial Wastewater Treatment. *Membranes (Basel)*. 2021;11(1):1-17. doi:10.3390/MEMBRANES11010066

30. Amirilargani M, Saljoughi E, Mohammadi T, Moghbeli MR. Effects of coagulation bath temperature and polyvinylpyrrolidone content on flat sheet asymmetric polyethersulfone membranes. *Polym Eng Sci*. 2010;50(5):885-893. doi:10.1002/PEN.21603

31. Lewis JA. BINDER REMOVAL FROM CERAMICS. *Annu Rev Mater Sci*. 1997;27:147-173. Accessed November 8, 2022. www.annualreviews.org

32. Anaya S, Serrano B, Herrero B, Cervera A, Baselga J. γ-Alumina Modification with Long Chain Carboxylic Acid Surface Nanocrystals for Biocompatible Polysulfone Nanocomposites. Published online 2014. doi:10.1021/am503744z

33. Kittaka S, Yamaguchi K, Takahara S. High physisorption affinity of water molecules to the hydroxylated aluminum oxide (0 0 1) surface. Published online 2011. doi:10.1016/j.jcis.2011.11.053

34. Hołda AK, Vankelecom IFJ. Understanding and guiding the phase inversion process for synthesis of solvent resistant nanofiltration membranes. *J Appl Polym Sci*. 2015;132(27). doi:10.1002/app.42130

35. Ren L, Luo X, Zhou H. The tape casting process for manufacturing low-temperature co-fired ceramic green sheets: A review. *Journal of the American Ceramic Society*. 2018;101(9):3874-3889. doi:10.1111/JACE.15694

36. Webb C, Khadke S, Schmidt ST, et al. pharmaceutics The Impact of Solvent Selection: Strategies to Guide the Manufacturing of Liposomes Using Microfluidics. doi:10.3390/pharmaceutics11120653

37. Cutler RA, Kleinlein B. Effect of the hydroxyl content and molecular weight of polyvinyl butyral on tape properties. *J Eur Ceram Soc*. 2009;29:3211-3218. doi:10.1016/j.jeurceramsoc.2009.06.020

38. Carrot C, Bendaoud A, Pillon C. Polyvinyl Butyral. In: ; 2015:89-137. doi:10.1201/b19190-4

39. Howard KE, Zyxw CD, Lakeman E, Payne DA. *Surface Chemistry of Various Poly(Vinyl Butyral) Polymers Adsorbed onto Alumina*. Vol 8.; 1990.

40. Cleary PW, Ha J, Prakash M, Nguyen T. Short shots and industrial case studies: Understanding fluid flow and solidification in high pressure die casting. *Appl Math Model*. 2010;34(8):2018-2033. doi:10.1016/J.APM.2009.10.015

41. Zhu X, Jiang D, Tan S. Improvement in the strength of reticulated porous ceramics by vacuum degassing. *Mater Lett*. 2001;51:363-367. Accessed November 14, 2022. www.elsevier.comrlocatermatlet

42. Li H, Zhang Y, Li C, et al. Extreme pressure and antiwear additives for lubricant: academic insights and perspectives. 1:3. doi:10.1007/s00170-021-08614-x

43. Rotella C, Persson BNJ, Scaraggi M, Mangiagalli P. Lubricated sliding friction: Role of interfacial fluid slip and surface roughness. Published online 2020. doi:10.1140/epje/i2020-11933-4

44. Vandezande P, Gevers LEM, Vankelecom IFJ. Solvent resistant nanofiltration: separating on a molecular level. doi:10.1039/b610848m

45. Ebrahimpour M, Safekordi AA, Mousavi SM, Nasab AH. Phase separation analysis in the ternary system of poly (butylene succinate) /1,1,2,2,-tetrachloethane/non-solvent in relation to membrane formation. *Bulgarian Chemical Communications*. 2017;49:389-395.

46. Research. HUMIC SUBSTANCES REMOVAL BY POLYSULFONE-BASED ULTRAFILTRATION MEMBRANE : A REVIEW. Published online 2015. doi:10.13140/RG.2.1.1094.0328

47. Zhu Z, Xiao J, He W, Wang T, Wei Z, Dong Y. A phase-inversion casting process for preparation of tubular porous alumina ceramic membranes. *J Eur Ceram Soc*. 2015;35(11):3187-3194. doi:10.1016/j.jeurceramsoc.2015.04.026

48. Smolders CA, Reuvers AJ, Boom RM, Wienk IM. *Microstructures in Phase-Inversion Membranes. Part 1. Formation of Macrovoids**. Vol 73. Elsevler Science Pubhshers; 1992.

49. Smolders CA, Reuvers AJ, Boom RM, Wienk IM. Microstructures in phase-inversion membranes. Part 1. Formation of macrovoids*. *Journal of Membrane Sctence*. 1992;73:259-275.

50. Dhaliwal AK, Hay JN. *The Characterization of Polyvinyl Butyral by Thermal Analysis*.

51. Yang TCK, Chang WH, Viswanath DS. ~RMAL DEGRADATION OF POLY(VINYL BUTYRAL) IN ALUMINA, MULLITE AND SILICA COMPOSITES. *Journal of Thetw~al Analysis*. 1996;47:697-713.

52. Goodyer CE, Bunge AL. Mass transfer through membranes with surface roughness. *J Memb Sci*. 2012;409:127-136. doi:10.1016/j.memsci.2012.03.043

53. Lik J, Chau H, Tellez C, Yeung KL, Ho K. The role of surface chemistry in zeolite membrane formation. *J Memb Sci*. 2000;164:257-275.

54. Hoek EM v, Bhattacharjee S, Elimelech M. Effect of Membrane Surface Roughness on Colloid-Membrane DLVO Interactions. Published online 2003. doi:10.1021/la027083c

55. Li K, Zhao Z. The effect of the surfactants on the formulation of UV-curable SLA alumina suspension. *Ceram Int*. 2017;43(6):4761-4767. doi:10.1016/j.ceramint.2016.11.143

56. Reed JS, Reed JS. *Principles of Ceramics Processing*. Wiley; 1995.

57. Jordan GW, Meiman JC. Materials & Equipment/Whitewares A Collection of Papers Presented at the 90th Annual Meeting and the 1988 Fall Meeting of the Materials & Equipment and Whitewares Divisions.

58. Pan Y, Li H, Liu Y, et al. Effect of Holding Time During Sintering on Microstructure and Properties of 3D Printed Alumina Ceramics. *Front Mater*. 2020;7. doi:10.3389/fmats.2020.00054

59. Chu Z, Jia C, Liu J, Ding R, Yuan G. Effects of sintering time on microstructure and properties of alumina foam ceramics. *Journal of Ceramic Science and Technology*. 2017;8(4):499-504. doi:10.4416/JCST2017-00028

60. *Sintering Key Papers*. Springer Netherlands; 1990. doi:10.1007/978-94-009-0741-6

61. García-Leiva MC, Ocaña I, Martínez-Esnaola JM, Martín-Meizoso A, Gil-Sevillano J, Fuentes M. *TENSILE AND DIAMETRICAL COMPRESSION TESTS OF SIGMA SM1140+ FIBRES*.

62. CERAMICS IN SEVERE ENVIRONMENTS.

63. Marion BH, Johnstcoe JK. *V»" ^S7} ^| A PARAMETRIC STUDY OF THE DIAMETRAL COMPRESSION TEST FOR CERAMICS m Ma*.

64. Wei J, Li J, Song X, Feng Y, Qiu T. Effects of solid loading on the rheological behaviors and mechanical properties of injection-molded alumina ceramics. Published online 2018. doi:10.1016/j.jallcom.2018.07.036

65. Wen J, Zeng T, Pan X, Zhong Z, Yu S, Cheng S. Effect of solid loading and carbon additive on microstructure and mechanical properties of 3D-printed SiC ceramic. *Int J Appl Ceram Technol*. 2022;19(6):3007-3016. doi:10.1111/IJAC.14172

66. Ismiati N, Darwis D. The effect of sintering temperature on the mechanical properties of ceramic. In: *Journal of Physics: Conference Series*. Vol 1763. IOP Publishing Ltd; 2021. doi:10.1088/1742-6596/1763/1/012094

67. Chengxin Z, Feng C, Yang • Xiang, Zhihang • Peng. Effects of sintering temperature on mechanical properties of alumina fiber reinforced alumina matrix composites. *J Solgel Sci Technol*. 2020;93:185-192. doi:10.1007/s10971-019-05192-z

68. Mouiya M, Bouazizi A, Abourriche A, et al. Effect of sintering temperature on the microstructure and mechanical behavior of porous ceramics made from clay and banana peel powder. *Results in Materials*. 2019;4. doi:10.1016/J.RINMA.2019.100028

69. Mohamed Ariff AH, Mohamad Najib MA, Mohd Tahir S, As'Arry A, Mazlan N. Effect of sintering temperature on the properties of porous Al2O3-10 wt% RHA/10 wt% Al composite. *https://doi.org/101080/2374068X20201785204*. 2020;7(3):417-428. doi:10.1080/2374068X.2020.1785204

70. Investigation of mechanical properties based on grain growth and microstructure evolution of alumina ceramics during two step sintering process. doi:10.1088/1757-899X/146/1/012046

71. Atkinson S. Precisely controlling the density of water filtration membranes increases their efficiency, shows research. *Membrane Technology*. 2021;2021(8):5-6. doi:10.1016/S0958-2118(21)00124-5

72. Mohazzabi P. Archimedes' Principle Revisited. *Journal of Applied Mathematics and Physics*. 2017;05(04):836-843. doi:10.4236/JAMP.2017.54073

73. Duan B, Shen T, Wang D. Effects of solid loading on pore structure and properties of porous FeAl intermetallics by gel casting. Published online 2018. doi:10.1016/j.powtec.2018.12.019

74. Michálek M, Michálková M, Blugan G, Kuebler J. Effect of carbon contamination on the sintering of alumina ceramics. *J Eur Ceram Soc*. 2018;38(1):193-199. doi:10.1016/J.JEURCERAMSOC.2017.08.011

75. Landek D, Ćurković L, Gabelica I, Mustafa MK, Žmak I. Optimization of sintering process of alumina ceramics using response surface methodology. *Sustainability (Switzerland)*. 2021;13(12). doi:10.3390/su13126739

76. Almomani MA, Shatnawi AM, Alrashdan MK. Effect of Sintering Time on the Density, Porosity Content and Microstructure of Copper – 1 wt. % Silicon Carbide Composites. *Adv Mat Res*. 2014;1064:32-37. doi:10.4028/www.scientific.net/amr.1064.32

77. Sun Z, Li B, Hu P, Ding F, Yuan F. Alumina ceramics with uniform grains prepared from Al 2 O 3 nanospheres. Published online 2016. doi:10.1016/j.jallcom.2016.07.122

78. Salissou Y, Panneton R. Pressure/mass method to measure open porosity of porous solids. *J Appl Phys*. 2007;101(12). doi:10.1063/1.2749486

79. Naftaly M, Tikhomirov I, Hou P, Markl D. Measuring open porosity of porous materials using thz-tds and an index-matching medium. *Sensors (Switzerland)*. 2020;20(11). doi:10.3390/s20113120

80. Org E. *Title INFLUENCE OF POROSITY ON THE MECHANICAL PROPERTIES OF LEAD ZIRCONATE-TITANATE CERAMICS Publication Date*.; 1976.

81. Lü Q, Dong X, Zhu Z, Dong Y. Environment-oriented low-cost porous mullite ceramic membrane supports fabricated from coal gangue and bauxite. *J Hazard Mater*. 2014;273:136-145. doi:10.1016/j.jhazmat.2014.03.026

82. Siddiqui MU, Fazal A, Arif M, Bashmal S. membranes Permeability-Selectivity Analysis of Microfiltration and Ultrafiltration Membranes: Effect of Pore Size and Shape Distribution and Membrane Stretching. doi:10.3390/membranes6030040

83. Daramola MO, Aransiola EF, Ojumu T v. Potential Applications of Zeolite Membranes in Reaction Coupling Separation Processes. *Materials*. 2012;5:2101-2136. doi:10.3390/ma5112101

84. Zentou H, Abidin ZZ, Yunus R, Radiah D, Biak A, Korelskiy D. processes Overview of Alternative Ethanol Removal Techniques for Enhancing

Bioethanol Recovery from Fermentation Broth. Published online 2019. doi:10.3390/pr7070458

85. Bedard R, Liu C. Recent Advances in Zeolitic Membranes. Published online 2018. doi:10.1146/annurev-matsci-070317

86. Li Q, Xu ZL, Yu LY. Effects of mixed solvents and PVDF types on performances of PVDF microporous membranes. *J Appl Polym Sci*. 2010;115(4):2277-2287. doi:10.1002/APP.31324

87. Chapman PD, Oliveira T, Livingston AG, Li K. Membranes for the dehydration of solvents by pervaporation. *J Memb Sci*. 2008;318:5-37. doi:10.1016/j.memsci.2008.02.061

88. Tanaka K, Yoshikawa R, Ying C, Kita H, Okamoto KI. Application of zeolite membranes to esterification reactions. *Catal Today*. 2001;67:121-125.

89. Peters T, Benes N, Buijs H, Vercauteren F, Keurentjes J. Thin high flux ceramic-supported PVA membranes. *Desalination*. 2006;200:24-28. doi:10.1016/j.desal.2006.03.233

90. Pina MP, Arruebo M, Felipe M, et al. A semi-continuous method for the synthesis of NaA zeolite membranes on tubular supports. *J Memb Sci*. 2004;244:141-150. doi:10.1016/j.memsci.2004.06.049

91. Belviso C, Lettino A, Cavalcante F. Influence of synthesis method on LTA time-dependent stability. *Molecules*. 2018;23(9). doi:10.3390/molecules23092122

92. Yu S, Kwon S, Na K. Synthesis of LTA zeolites with controlled crystal sizes by variation of synthetic parameters: Effect of Na+ concentration, aging time, and hydrothermal conditions. *J Solgel Sci Technol*. 2021;98(2):411-421. doi:10.1007/s10971-018-4850-4

93. Malakian A, Zhou Z, Messick L, Spitzer TN, Ladner DA, Husson SM. membranes Understanding the Role of Pattern Geometry on Nanofiltration Threshold Flux. doi:10.3390/membranes10120445

94. Elimelech M, Zhu X, Childress AE, Hong S. Role of membrane surface morphology in colloidal fouling of cellulose acetate and composite aromatic polyamide reverse osmosis membranes. *J Memb Sci*. 1997;127:101-109.

95. Medesi AJ, Nötzel D, Hanemann T. materials PVB/PEG-Based Feedstocks for Injection Molding of Alumina Microreactor Components. doi:10.3390/ma12081219